Sterically stabilized (Zr,Ti)-(Al,Sn,Pb,Bi)-C MAX phase solid solutions with Zn additions and enhanced chemical complexity on the A-site

Nick Goossens[a,b*], Bensu Tunca[a], Michael Stuer[b], Per O.Å. Persson[c], Jin Won Seo[a], Shuigen Huang[a], Konstantina Lambrinou[d], Jozef Vleugels[a]

[a] *Department of Materials Engineering, KU Leuven, Kasteelpark Arenberg 44, BE-3001 Heverlee, Belgium*

[b] *Laboratory for High Performance Ceramics, Empa, Überlandstrasse 129, CH-8600, Dübendorf, Switzerland*

[c] *Department of Physics, Chemistry, and Biology (IFM), Linköping University, SE-58183, Linköping, Sweden*

[d] *School of Computing and Engineering, University of Huddersfield, Queensgate, Huddersfield HD1 3DH, United Kingdom*

* Corresponding author (nick.goossens@empa.ch)

Table of Contents figure

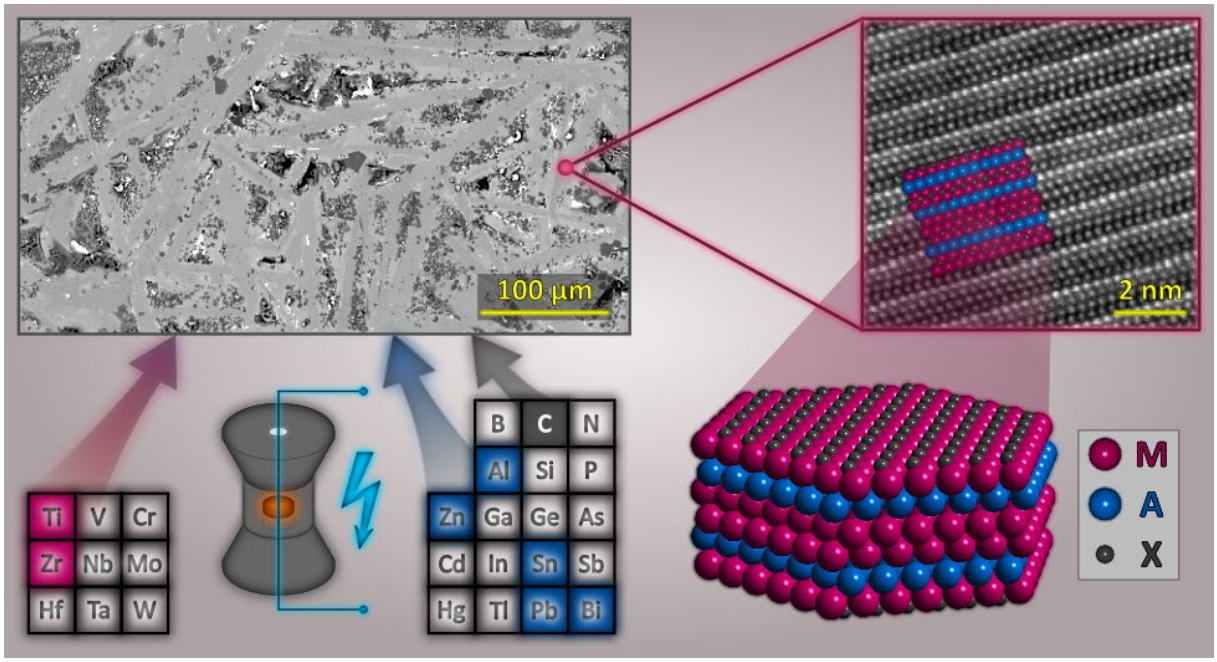

Abstract

The MAX phases constitute a family of nanolaminated ternary carbides and nitrides renowned for their compositional versatility, as reflected in the easy formation of solid solutions with variable chemical complexity. Synthesizing MAX phase solid solutions with intentionally tailored chemical complexity can produce materials that are able to meet the property requirements of the targeted application(s). This work presents an effective strategy specifically developed to design and fabricate highly phase-pure ceramics based on chemically complex MAX phase solid solutions by sterically stabilizing their unit cells. Steric unit cell stabilization is achieved via a judicious balance of dissimilar M- & A-elements, which targets the minimization of lattice distortions. This work produced high-purity (up to 88.7 wt.%) $(Zr_{0.8},Ti_{0.2})_2(Al,Sn,Pb)C$ and $(Zr_{0.8},Ti_{0.2})_2(Al,Sn,Pb,Bi)C$ 211 MAX phase solid solutions by spark plasma sintering at 1350-1500 °C. Molten Zn- and/or Pb/Bi-containing intermetallics facilitated the synthesis of soft (3-5 GPa), coarse-grained (length >20 μm, thickness >10 μm), and damage-tolerant ceramics. Intermetallics comprising Zn, Pb, and Bi improved (a) C/carbide dissolution, (b) Sn/C diffusion, and (c) carbide wetting, thus producing the 312 $(Zr_{0.8},Ti_{0.2})_3(Al,Sn,Pb,Bi)C_2$ MAX phase solid solution. Forming $(Zr_{0.8},Ti_{0.2})_3(Al,Sn,Pb,Bi)C_2$ contributed to the growth of very large platelets (length >100 μm) with distinct (312-core)/(211-shell) morphology. Zn did not occupy the A-site, unlike Al, Sn, Pb, and Bi. Sterically balanced A-site elemental occupancies, albeit non-equimolar, alleviated lattice distortions and aided the steric stabilization of the crystal structure, whereas the chemical complexity on the A-site increased the configurational entropy of the synthesized MAX phase compounds, despite pre-existing M-site compositional restrictions, further enhancing their thermodynamic stability.

Keywords

High-entropy ceramics, MAX phase synthesis, reactive powder sintering, spark plasma sintering, chemically complex solid solutions, metal hydrides

1. Introduction

The $M_{n+1}AX_n$ (MAX) phases are a family of nanolaminated ceramics consisting of an early transition metal (M), an A-group element (A, mainly, groups 11-16 in the periodic table), and carbon or nitrogen (X), while the number n is an integer typically smaller than 4.[1] The MAX phases are hexagonal solids (space group $P6_3/mmc$) with unit cells comprising covalently bonded M_6X octahedra and metallically bonded M_6A trigonal prisms. Their mixed chemical bonding and crystal structure nanolamination endow the MAX phases with rather special thermomechanical properties, some of them characteristic of ceramics and some of metals. This means that the MAX phases are soft, damage-tolerant, machinable, and deformable (properties typical of metals), as well as stiff, strong, chemically inert, and able to retain their mechanical properties at elevated temperatures (properties typical of ceramics).[2, 3] The excellent performance of high-purity MAX phase ceramics in harsh service environments (e.g., corrosive media, high temperatures, irradiation) is promising for their exploitation within the context of clean energy production and storage. Coupling energy harvesting by concentrated solar power (CSP) with thermal energy storage (TES) employs corrosive molten salts at high temperatures as main heat transfer fluids (HTFs), thus demanding corrosion mitigation strategies for components exposed to HTFs.[4-7] The corrosion susceptibility of most metallic alloys, in bulk or coating form, dictates the choice of HTF and narrows the operation 'window' of CSP/TES systems, thereby limiting their operational efficiency. Similarly, the deployment of Gen-IV nuclear systems, such as lead-cooled fast reactors (LFRs) and (thorium, Th) molten salt reactors (MSRs), relies on the reliable performance of structural and fuel cladding materials (typically steels) under extremely harsh service conditions combining inherently corrosive coolants (e.g., liquid lead, Pb; lead-bismuth eutectic, LBE; molten salts), high nominal temperatures (>600 °C), and neutron irradiation.[8-10] The efficiency of these nuclear power systems is currently limited by the rate at which most candidate structural/functional metallic alloys degrade (i.e., corrode and/or embrittle) in contact with heavy liquid metals or molten salts.[11] The MAX phases have demonstrated excellent compatibility with both types of corrosive media (even at high liquid metal flow velocities promoting erosion)[12] in combination with a remarkable tendency for dynamic recovery of radiation-induced defects, especially above 600 °C.[12-19] Therefore, MAX phase ceramics are promising candidate materials for CSP and next-generation nuclear systems (both fission and fusion), including their prospective use as coatings for accident-tolerant fuel (ATF) claddings used in Gen-II/III light water reactors (LWRs). As the radiation tolerance of non-optimized MAX phase ceramics is known to be less ideal at Gen-II/III LWR nominal operation temperatures (i.e., 280-340 °C),[16, 17] sophisticated materials engineering strategies must be adopted to fabricate 'nuclear grade' MAX phase ceramics, which ideally combine high phase-purity, fine grains, and strongly textured microstructures.[20-23] The design of innovative materials for applications near the nuclear reactor

core (e.g., fuel cladding coatings) must obey additional criteria, such as the selection of elements with small neutron cross-sections (e.g., zirconium, Zr) and/or elements that are less susceptible to transmutation during reactor service. In case the use of elements with large neutron cross-sections (e.g., hafnium, Hf; tantalum, Ta; etc.) cannot be avoided, one should be prepared to pay the associated 'neutronic penalty' through fuel enrichment.

Knowing the ideal MAX phase stoichiometry for a specific nuclear application is not sufficient for the synthesis of phase-pure ceramics, as demonstrated by the 'difficult' Zr-Al-C and Hf-Al-C ternary systems, where the highest reported MAX phase contents were 67 wt.% for Zr_2AlC,[24, 25] 61 mol.% for Zr_3AlC_2,[26] and 49 wt.% for Hf_2AlC & Hf_3AlC_2[27, 28] produced via a powder metallurgical route involving pressure-assisted densification. In these systems, significant fractions of competing phases, such as binary carbides (e.g., ZrC, HfC) and binary intermetallics (e.g., $ZrAl_2$, $HfAl_2$), and/or the lack of texture can compromise the structural integrity of MAX phase ceramics under irradiation due to differential and anisotropic radiation-induced swelling, respectively.[16, 18, 19, 29] Several strategies aiming at high phase-purity have been developed to accelerate the diffusion-controlled reaction kinetics of the MAX phase constituent elements. One strategy involves the use of fine-grained, oxidation-resistant precursors, such as finely milled metal hydride powders.[27, 30] A second strategy relies on the judicious design of double solid solution MAX phases (i.e., solid solutions on both M- & A-sites), whereby the appropriate alloying elements are introduced into the M-& A-sites to balance out critical distortions of the MAX phase unit cell stemming from sterically mismatched elements; such distortions can result in MAX phase decomposition and the concurrent formation of large fractions of undesirable parasitic phases.[31-33] Moreover, solid solution synthesis permits tailoring of MAX phase properties, including their resistance to corrosive media and irradiation.[12, 15, 23, 25, 31-36] Secondary phases affect adversely the oxidation and corrosion resistance of MAX phase ceramics and must be avoided.[14] Intermetallics are highly susceptible to corrosion/oxidation in contact with oxygen-containing liquid metals, whilst grain boundaries and stacking faults in otherwise corrosion-immune (pseudo)binary carbides act as preferred paths for the ingress of liquid metals into the material bulk,[12, 14, 25] degrading the corrosion resistance of MAX phase ceramics intended for use in contact with liquid metal coolants. The existing possibilities of tuning structural, mechanical, electronic, optical, and magnetic properties through the rational design of MAX phase solid solutions have been explored using diverse computational approaches.[37-42] In practice, MAX phase solid solutions must be judiciously tailored for stability under the targeted service conditions. As a rule of thumb, small M-elements are more compatible with small A-elements and *vice versa*; this is exemplified by the extremely difficult synthesis of Zr_2AlC when compared to Zr_2SnC and by the proven stabilization of Zr_2AlC through the formation of $Zr_2(Al,Sn)C$ solid solutions.[31, 33, 43] More recently, the enhanced configurational entropy of chemically complex 'high-entropy carbides' (HECs) was held partly

accountable for their structural stabilization – a strategy perfectly transferable to the MAX phases.[44, 45] As mentioned earlier, the design of chemically complex MAX phase solid solutions might be subjected to (application-specific) restrictions vis-à-vis elemental selection; an example is the preferred exclusion of M-elements with large neutron cross-section from candidate coating materials of nuclear fuel cladding tubes.

MAX phase solid solutions utilizing the A-site have been explored much less than M-site solid solutions and have predominantly focused on binary (Al,A) combinations with A = Si, Ga, Ge, In, Sn, Sb, Pb, Bi.[31-33, 43, 46-50] Most A-site (double) solid solutions relied on the (Al,Sn) pair, as both elements are sterically complementary; this pair is compatible with virtually every M-element, and the resulting solid solutions are easily processed via conventional reactive powder sintering methods.[31-33] Apart from Sn (T_m(Sn) ≈ 231.9 °C), other low-melting-point A-elements (e.g., Ga, T_m(Ga) ≈ 29.8 °C; In, T_m(In) ≈ 156.6 °C; Bi, T_m(Bi) ≈ 271.5 °C; and Pb, T_m(Pb) ≈ 327.5 °C) are less straightforward to process due to liquid phase formation that either results in difficult to prevent material losses or requires non-conventional processing approaches based on the (partial) substitution of one A-element (usually Al) by another via molten salts (e.g., Cu, Zn)[25, 51-55] or liquid metals (e.g., Pb, Bi).[25, 54, 55] Substitution processes often rely on the destabilization (e.g., 'corrosion attack') of the precursor MAX phase through chemical reactions with the corrosive medium; such processes are rarely possible to control and the exact reaction paths are very difficult to predict.

Inspired by the chemistry of typical corrosion media, such as liquid Pb & LBE used as primary coolants of Gen-IV LFRs, we formulated potential MAX phase solid solution compositions based on A-elements (Al, Zn, Sn, Pb, Bi) that partake in corrosion-induced elemental substitution reactions,[25] and attempted to synthesize these solid solutions via reactive powder sintering. It is worthwhile to note that the proactive reconciliation of the chemistries of the MAX phases and the corrosive media to which they are exposed has the potential to become an effective liquid metal corrosion mitigation strategy vis-à-vis the prospective use of MAX phases in contact with molten salts and liquid metals. This hypothesis is based on the idea of 'pre-saturating' the MAX phase compound with elements found in a specific corrosive medium, thus preventing *in situ* A-element partial substitution reactions during service, a phenomenon that has been observed during the exposure of Zr_2AlC-based ceramics to oxygen-poor liquid LBE at 500 °C.[12, 25] This work demonstrates that the design and synthesis of chemically complex A-site MAX phase solid solutions is an interesting – yet unexplored – approach for the fabrication of high-purity MAX phase ceramics able to meet the stringent property requirements of energy applications that demand reliable material performance in contact with corrosive media (i.e., liquid metals, molten salts). This approach is showcased in this work by the successful synthesis of quasi phase-pure

211 MAX phase solid solutions with enhanced chemical complexity on the A-site in the $(Zr_{0.8},Ti_{0.2})$-(Al,Sn,Pb,Bi)-C system.

2. Materials and Methods

2.1 Feedstock powders

The characteristics of the feedstock (raw) powders used in this work are summarized in **Table 1**. The lead-bismuth eutectic (LBE; 55.3 wt.% Bi, 44.7 wt.% Pb) was supplied as a solid metal block, which was drilled into turnings; the turnings were subsequently crushed with pestle and mortar, after their embrittlement in liquid nitrogen (N_2), until small flakes (<1 mm) were obtained. The exact composition and impurities of solid LBE are reported elsewhere.[9]

Table 1. Overview of the starting powders used in this work.

Powder	Grain size	Purity	Supplier	Origin
Zirconium hydride (ZrH_2)	<6 μm	>99%	Chemetall	Germany
Titanium hydride (TiH_2)	<2 μm	>99%	Chemetall	Germany
Aluminum (Al)	<5 μm	>99%	Atlantic Equip Eng§	USA
Tin (Sn)	<5 μm	99.9%	Atlantic Equip Eng§	USA
Zinc (Zn)	<15 μm	>99 %	Nyrstar	Belgium
Lead (Pb)	<150 μm	99.5%	Abcr GmbH	Germany
Lead-bismuth eutectic (LBE)	Solid metallic ingot (exact composition in [9])			
Graphite (C)	<5 μm	>99%	Asbury Graphite Mills	USA

§ Atlantic Equip Eng = Atlantic Equipment Engineers

2.2 Reactive powder sintering of chemically complex MAX phase solid solutions

All starting powder mixtures were prepared by weighing and dry-mixing the individual powder components in non-stoichiometric ratios, using a polyethylene container under protective argon (Ar) atmosphere in a Turbula mixer (24 h, 75 rpm). Deviations from the ideal 211 stoichiometry (M:A:X elements in the 2:1:1 ratio) typify 211 MAX phase synthesis; these deviations aim at compensating possible liquid phase losses that occur during pressure-assisted densification and suppressing excessive (pseudo)binary carbide formation by adding excess A-element(s) and deficient carbon (C), since both binary and ternary carbides can accommodate up to 30 at.% of C vacancies. The starting powder mixtures had the $(Zr_{0.8},Ti_{0.2})_2(Al_{0.25},Zn_{0.25},Sn_{0.25},Pb_{0.25})_{1.05}C_{0.95}$,

$(Zr_{0.8},Ti_{0.2})_2(Al_{0.25},Sn_{0.25},LBE_{0.5})_{1.05}C_{0.95}$ and $(Zr_{0.8},Ti_{0.2})_2(Al_{0.2},Zn_{0.2},Sn_{0.2},LBE_{0.4})_{1.05}C_{0.95}$ nominal stoichiometries, herein referred to as 'Pb*x*', 'LBE*x*', and 'Zn*x*', respectively, with *x* denoting the sintering temperature. All starting powder mixtures targeted the fabrication of 211-type MAX phase solid solutions with equimolar A-site chemistries. The subsequent densification of the starting powder mixtures made use of a cylindrical graphite die/punch setup (∅ 30 mm) with graphite paper (acting as release aid) covering the inner surfaces of the powder chamber. Manual cold compaction (30 kN) of the feedstock powder mixture using a uniaxial hand press preceded their final consolidation by spark plasma sintering (SPS; HP D 25, FCT Systeme) in an actively pumped vacuum. The sintering cycle consisted of a quick (50 °C min^{-1}) initial heating – by internal Joule heating due to the application of a pulsed current (10/2 ms on/off) at 9 kA and 10 V – under a minimal force (5 kN) up to the specified sintering temperature (1350/1450/1500 °C), followed by a dwell period (1 h) under pressure (40 MPa), and concluded with natural cooling in vacuum without any applied force. Vigorous sand blasting of the sintered discs allowed the detachment of residual graphite paper prior to final two-sided grinding and polishing to remove any hard surface reaction layers rich in (pseudo)binary carbides.

2.3 Characterization of MAX phase ceramics

The density (ρ) of the MAX phase solid solution ceramics was determined via the Archimedes principle. The Vickers hardness (H_V) was measured using an indentation load of 3 kg for 15 s, using a Future Tech model FV700.

The constituent phases of the sintered disc-shaped MAX phase ceramics were determined by X-ray diffraction (XRD; Rigaku SmartLab SE system equipped with 1D/teX Ultra 250 HE detector), using Cu-K_α radiation (40 kV, 40 mA) in a Bragg-Brentano geometry. The XRD patterns were acquired in the 5-90° 2θ range in steps of 0.04° and at a speed of 0.1° min^{-1} using a 10 mm length-limiting slit. The crystallography and diffraction response of all constituent phases were initially simulated using the VESTA v.3.5.8 software and were subsequently utilized to perform the full structural Rietveld refinement of all phases, including lattice parameters and atomic positions, using the Profex v.5.4.1 software.

The microstructure and chemical composition of metallographic cross-sections of the MAX phase ceramics were investigated using scanning electron microscopy (SEM; FEI Nova NanoSEM 450) in the backscattered electron (BSE) mode and in conjunction with energy-dispersive X-ray spectroscopy (EDS) for elemental analysis. Elemental mapping was performed using electron probe microanalysis (EPMA; JEOL JXA-8530F) equipped with a wavelength-dispersive X-ray spectroscopy (WDS; 1-5 eV, 8 eV at Fe-K_α, full scanner type spectrometer) detector. Additional EDS elemental analysis (1 SDD/UTW, 129 eV at Mn-K_α) of the identified phases was performed on the same device at fixed conditions (i.e., 15 kV accelerating voltage, 100 nA beam current).

Focused ion beam (FIB; FEI Nova 600 NanoLab Dual Beam FIB/SEM) was used to lift out thin foils (thickness <100 nm) from metallographic cross-sections of the MAX phase ceramics, following the classic lift-out method. Atomically resolved high-angle annular dark-field (HAADF) scanning transmission electron microscopy (STEM) images and lattice-resolved elemental maps of the thin films were acquired with a double Cs-corrected, monochromated FEI Titan^3 60-300, equipped with a Super-X EDS detector for elemental mapping, operated at 300 kV, and with a probe-lens aberration-corrected JEOL JEM-ARM200F equipped with a cold field emission gun (FEG), operated at 200 kV.

3. Results and Discussion

3.1 MAX phase formation in the (Zr,Ti)-(Al,Zn,Sn,Pb)-C system

Spark plasma sintering the $(Zr_{0.8},Ti_{0.2})_2(Al_{0.25},Zn_{0.25},Sn_{0.25},Pb_{0.25})_{1.05}C_{0.95}$ starting powder mixture at 1350 °C (Pb1350), 1450 °C (Pb1450), and 1500 °C (Pb1500) produced ceramic discs with distinct metal-like luster that did not exhibit visible surface pores or cracks. Rietveld structural refinement based on their individual XRD patterns (Figure 1a-c) revealed an appreciable phase-purity (>80 wt.%) with a 211 MAX phase as the principal phase, and (Zr,Ti)C as the main competing phase. The Rietveld-refined profiles were used to compile a list of calculated d-spacings, 2θ angles, and relative diffraction intensities of the observed MAX phases (Supporting Information, SI, Tables S1-S3). BSE images (Figure 1d; SI Figure S1) revealed that the fine (Zr,Ti)C carbide particles (dark contrast) were well-dispersed in the coarse-grained platelet-shaped MAX phase matrix. Minor impurity phases appearing in the microstructure but not detected by XRD were small alumina (Al_2O_3) grains and intermetallic (IMC) phases segregating in grain boundaries (GBs) and triple junctions (Figure 1e). Remarkably, the MAX phase grains coarsened considerably (20-30 μm in length, 5-10 μm in thickness), indicating favorable elemental diffusion involved in their formation and growth, especially at the highest synthesis temperature. Moreover, grain coarsening resulted in soft (4-5 GPa; Table 2) and damage-tolerant ceramics, evidenced by extensive MAX phase platelet delamination, kinking, and material dislodging in response to Vickers indentation (Figure 1f; SI Figure S1c,f), as well as resistance to crack formation and propagation. Despite aiming for an equimolar A-site occupancy, SEM/EDS analysis revealed a strong and consistent deficiency in Zn and Pb in the MAX phase grains (Table 2). Since XRD proved to be insufficiently accurate for structural refining of the site occupancies, the atomic stacking was directly investigated by (S)TEM. First, the STEM analysis of the MAX phase grains (Figure 1g,h) confirmed the zigzag atomic stacking along the *c*-axis characteristic of the MAX phases. Remarkably, the lattice switched abruptly from a 211 (M-M-A-M-M) to a 312 (M-M-M-A-M-M-M)

atomic stacking, revealing the local initiation of an $M_2AC \rightarrow M_3AC_2$ phase transformation. Except for the unreported Ti_3PbC_2, the $M_2AC \rightarrow M_3AC_2$ (M = Ti or Zr; A = Al, Sn, or Pb) phase transition is known to proceed at higher SPS processing temperatures, often in conjunction with the formation of liquid phases that assist elemental diffusion and grain coarsening.[36, 52, 56] Second, TEM/EDS (Figure 1i) unambiguously proved the partial A-site occupancy by Pb, whereas Zn was not incorporated in the structure, segregating into IMC GB phases, locations at which SEM/EDS picked up the Zn signal. Therefore, Zn is believed to favor liquid phase formation, similar to Fe, Co, and Ni.[56]

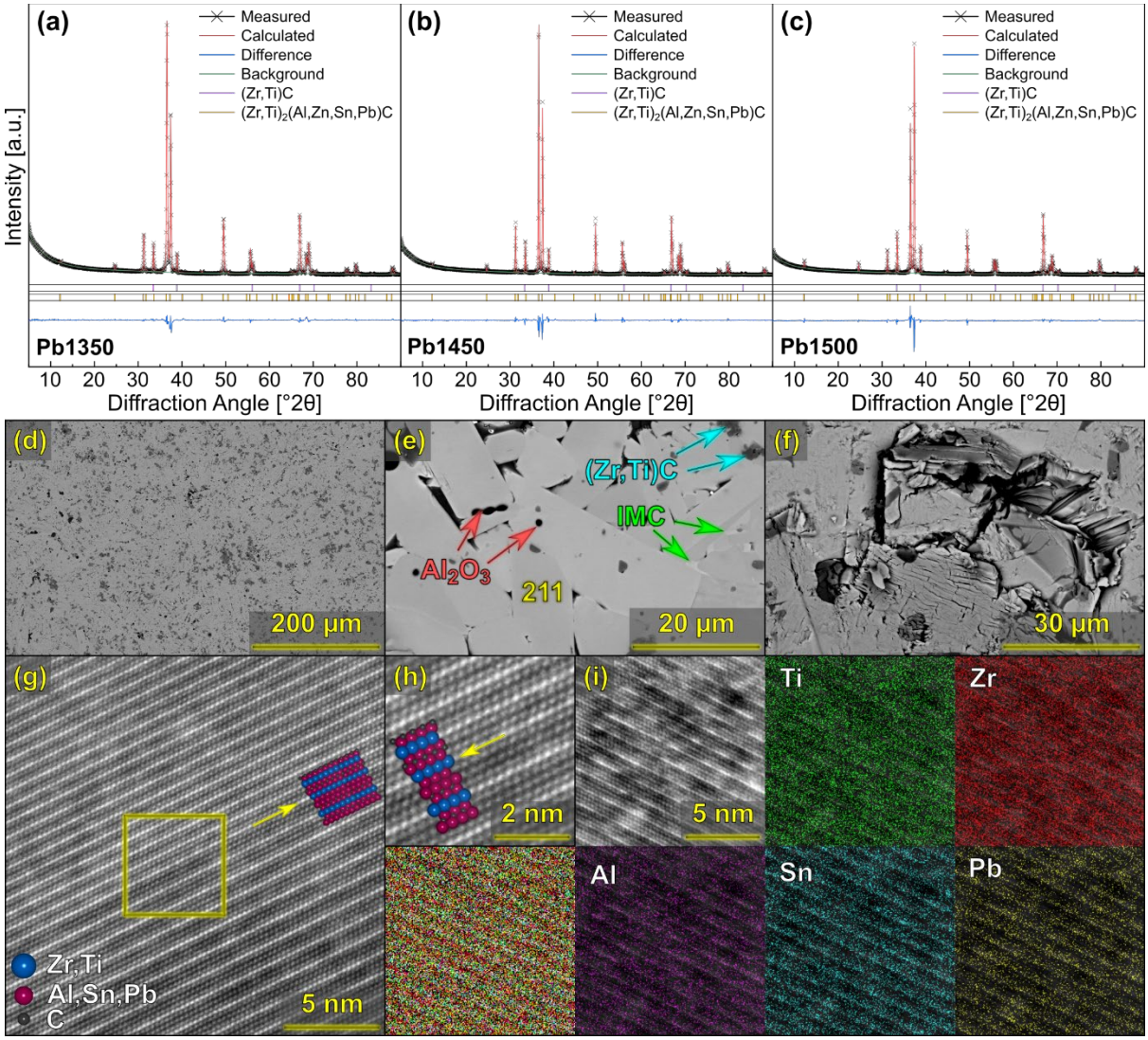

Figure 1. XRD patterns and Rietveld structural refinement of (a) Pb1350, (b) Pb1450, and (c) Pb1500 MAX phase ceramics in the (Zr,Ti)-(Al,Zn,Sn,Pb)-C system. SEM analysis (BSE, 20 kV) of Pb1350 revealed (d,e) characteristic MAX phase platelets and minor impurities; and (f) MAX phase delamination indicating damage tolerance near a Vickers indentation. STEM analysis of Pb1350 showed (g,h) 211-to-312 atomic stacking transition along the *c*-axis ([$11\bar{2}0$] zone axis, Z.A.; atomic models superimposed); and (i) homogeneous elemental distribution in the M- & A-layers (HAADF STEM/EDS elemental maps of single Ti, Zr, Al, Sn, Pb, and their superposition).

Table 2. Rietveld-refined structure, chemical composition, and physical properties of the sintered ceramics. **Bold digits** denote the uncertainties.

	Pb1350		**Pb1450**		**Pb1500**		**LBE1350**		**LBE1450**		**LBE1500**	
Phase	211	MC	211	MC	211	MC	211	MC	211	MC	211	MC
[wt.%]*	88.7	11.3	83.1	16.9	81.0	19.0	62.3	37.7	81.8	18.2	72.8	27.2
R_w [%]	2.91		3.54		3.38		5.39		3.14		5.96	
Lattice parameters (Rietveld-refined)												
a [Å]	3.303**2**	4.633**6**	3.301**0**	4.635**2**	3.305**8**	4.639**2**	3.322**0**	4.634**1**	3.316**2**	4.630**7**	3.319**4**	4.627**6**
c [Å]	14.426**5**		14.420**1**		14.432**3**		14.443**5**		14.431**7**		14.432**1**	
V [Å^3]	136.321	99.485	136.079	99.588	136.590	99.846	138.039	99.517	137.445	99.298	137.714	99.099
c/a	4.367		4.368		4.366		4.348		4.352		4.348	
z_M	0.0849**9**		0.0851**6**		0.0853**8**		0.0853**8**		0.0848**9**		0.0855**1**	
Elemental analysis (SEM/EDS)												
M-site [at.%]												
Ti	26.0	16.9	26.8	15.5	24.8	16.1	21.5	18.7	22.0	19.6	22.6	16.0
Zr	74.0	83.1	73.2	84.5	75.2	83.9	78.5	81.3	78.0	80.4	77.4	84.0
A-site [at.%]												
Al	33.1		35.8		28.9		35.9		39.9		41.0	
Zn	8.1		5.9		15.2							
Sn	47.2		48.2		45.4		38.1		33.6		32.7	
Pb	11.6		10.1		10.5		15.5		15.3		14.6	
Bi							10.5		11.2		11.7	
ρ [g cm^{-3}]	6.7**2**		6.7**3**		6.8**3**		7.0**2**		7.0**4**		7.3**2**	
H_V [GPa]	4.1 ± 0.1		4.9 ± 0.2		4.8 ± 0.1		4.0 ± 0.1		3.6 ± 0.3		3.6 ± 0.1	

* LBE1500 and Zn1350 contained trace quantities of metallic Bi.

Table 2 (ctd.)**.** Rietveld-refined structure, chemical composition, and physical properties of the sintered ceramics. **Bold digits** denote the uncertainties.

	Zn1350			**Zn1450**		**Zn1500**	
Phase	211	312	MC	211	MC	211	MC
[wt.%]*	36.7	35.2	28.1	47.7	52.3	67.8	32.2
R_w [%]		5.29			5.01		4.27
Lattice parameters (Rietveld-refined)							
a [Å]	3.318**2**	3.326**2**	4.642**8**	3.323**1**	4.642**4**	3.318**1**	4.635**4**
c [Å]	14.416**1**	19.726**3**		14.449**3**		14.431**5**	
V [Å^3]	137.462	189.005	100.078	138.186	100.052	137.601	99.601
c/a	4.345	5.931		4.348		4.349	4.367
z_M	0.0855**5**	0.1284**5**		0.0852**0**		0.0844**8**	
z_X		0.0707**2**					
Elemental analysis (SEM/EDS)							
M-site [at.%]							
Ti	22.4	15.9	15.9	22.3	19.5	20.1	13.8
Zr	77.6	84.1	84.1	77.7	80.5	79.9	86.2
A-site [at.%]							
Al	24.9	22.2		28.4		37.6	
Zn	7.2	6.4		3.5		10.6	
Sn	43.5	45.7		38.8		37.3	
Pb	16.1	16.9		18.6		3.1	
Bi	8.3	8.8		10.7		11.4	
ρ [g cm^{-3}]		6.6**4**			6.9**2**		7.0**3**
H_V [GPa]		2.9 ± 0.2			4.3 ± 0.3		4.3 ± 0.1

* LBE1500 and Zn1350 contained trace quantities of metallic Bi.

Materials processing in vacuum comes with the intrinsic risk of losing low-melting-point A-elements through liquid/vapor phase formation (see SI Table S4 for relevant vapor pressures, P_{vap}) during heating, thus promoting the formation of M_3AC_2/MC phases as the powder mixture becomes progressively A-element-deficient. Similarly, exposing certain M_2AC phases (notably, Ti_2AlC[57] and Hf_2AlC[27]) to high-temperature vacuum confines their decomposition within their respective M_3AC_2 phase. Regardless of the synthesis temperature, XRD could not detect the M_3AC_2 phase in the bulk ceramic, supporting the hypothesis of its local (low volume fraction) confinement. Therefore, the $(Zr,Ti)_2(Al,Sn,Pb)C$ MAX phase solid solution should be considered thermally stable within the 1350-1500 °C range.

3.2 MAX phase formation in the (Zr,Ti)-(Al,Sn,Pb,Bi)-C system

Earlier observations of LBE penetration into Zr_2AlC to form *in situ* a $Zr_2(Al,Pb,Bi)C$ solid solution inspired our approach to intentionally synthesize a Zr-based MAX phase with LBE as a starting reagent.[25] Assuming that the low-melting-point LBE (T_m(LBE) ≈ 123.5 °C) could provide a suitable liquid environment favoring A-site solid solutioning, Zn was not added to the system. Similar to the Pb*x* series, the SPS densification of the $(Zr_{0.8},Ti_{0.2})_2(Al_{0.25},Sn_{0.25},LBE_{0.5})_{1.05}C_{0.95}$ starting powder mixture at 1350 °C (LBE1350), 1450 °C (LBE1450), and 1500 °C (LBE1500) resulted in visibly dense, crack-free discs with metallic luster. Despite having comparable XRD patterns (Figure 2a-c) and phase assemblies (i.e., a 211-type MAX phase and (Zr,Ti)C impurities, see Table 2), all LBE*x* ceramics contained generally lower and more variable MAX phase fractions (<82 wt.%) than their Pb*x* counterparts. The Rietveld-refined XRD profiles were used to compile a list of calculated d-spacings, 2θ angles, and relative diffraction intensities of the observed MAX phases (SI Tables S5-S7). The microstructure (Figure 2d, SI Figure S2) consisted of large MAX phase platelets (bright BSE contrast) and locally clustered, fine (Zr,Ti)C particles (dark BSE contrast), suggesting similarly favorable diffusion kinetics promoting fast MAX phase formation and growth. Sparsely dispersed LBE 'islands' (bright BSE contrast, Figure 2e) were observed despite the low melting point of Pb/Bi-based alloys, especially near the eutectic composition. Intriguingly, two weeks of sample storage at room temperature (RT) caused distinctive Bi-rich whisker formation (Figure 2f); the whiskers nucleated in LBE 'islands' and emerged out of the polished sample surface. The RT transformation of solidified LBE into a closed-packed β-Pb_7Bi_3 phase (*hcp*, 11.17 g cm^{-3}) and a less dense γ phase (Bi with 0.4 wt.% Pb; *rhombohedral*, 9.747 g cm^{-3}) has been previously reported.[58] This post-freezing LBE phase transformation is accompanied by a volume expansion, subjecting the γ-Bi phase to compressive stresses that result in its exudation from the sample surface and the formation of Bi-rich hillocks.[58-60]

The addition of Pb and Bi densified (7.0-7.4 g cm^{-3}) and softened (3.6-4.0 GPa) the MAX phase solid solutions, despite the presence of more pronounced (Zr,Ti)C clusters. Moreover, Vickers

indentation of the generally softer LBE*x* ceramics (Figure 2g; SI Figure S2c,f) resulted in more extensive dislodging, MAX phase delamination, and kinking as compared to the Pb*x* ceramics sintered at the same temperatures (Figure 1f; SI Figure S1c,f). Although both SEM/EDS (Table 2) and EPMA/WDS (Figure 2h) confirmed larger Pb (and Bi) fractions in the LBE*x* MAX phase solid solutions as compared to the Pb*x* ceramics, the intended equimolar A-site occupancy was not achieved. Nonetheless, alloying the A-site with ~1/3 of large and heavy Pb/Bi caused the *a* and (to a lesser extent) *c* lattice parameters to increase accordingly.

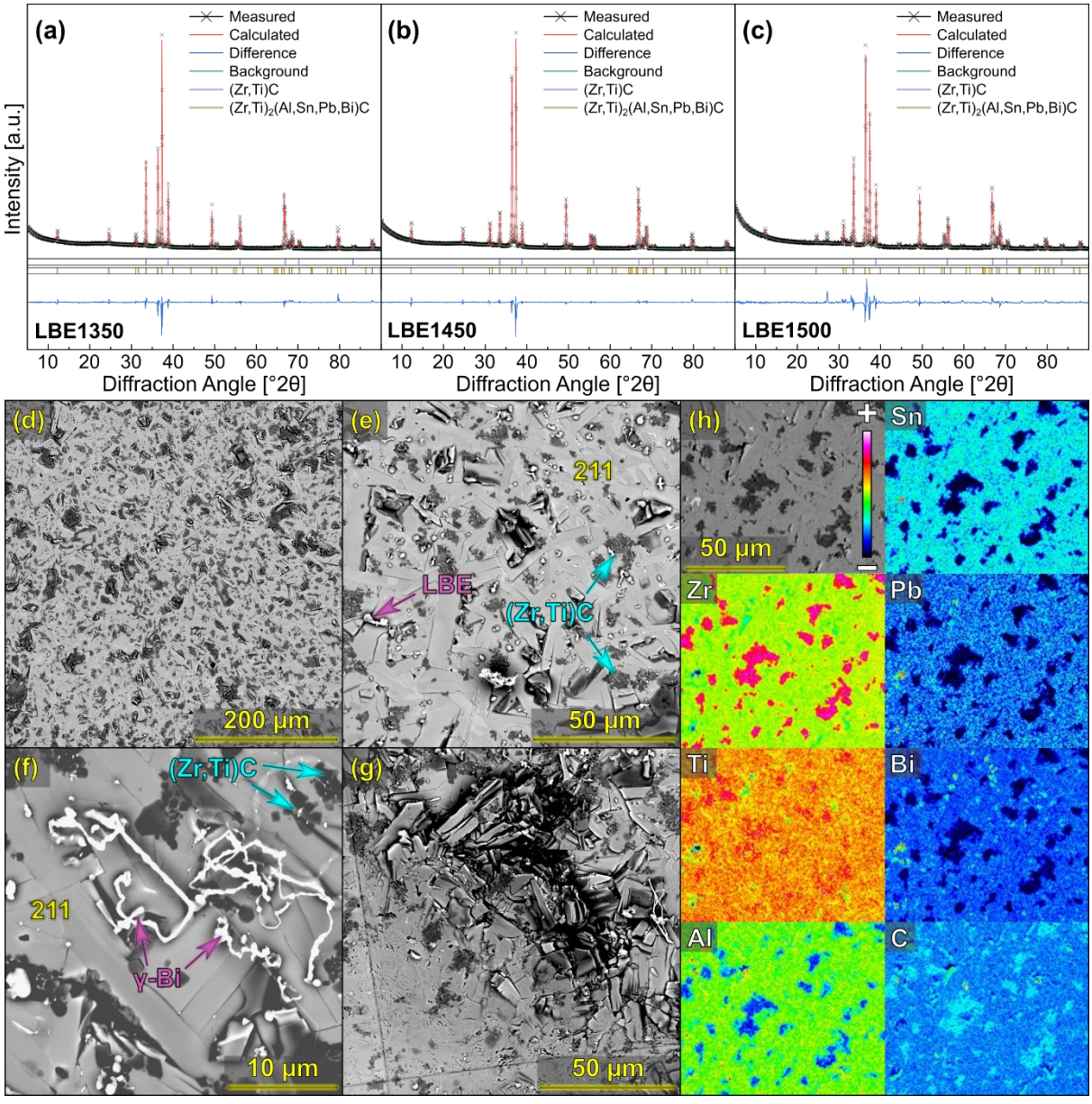

Figure 2. XRD patterns and Rietveld structural refinement of (a) LBE1350, (b) LBE1450, and (c) LBE1500 MAX phase ceramics in the (Zr,Ti)-(Al,Sn,Pb,Bi)-C system. SEM analysis (BSE, 20 kV) of LBE1450 revealed (d,e) characteristic MAX phase platelets and minor impurities; (f) Bi whisker emergence from the polished surface after RT storage (14 days); and (g) MAX phase delamination indicating damage tolerance near a Vickers indentation. (h) EPMA/WDS elemental mapping of LBE1450 confirmed the homogeneous elemental distribution in the MAX phase grains.

3.3 MAX phase formation in the (Zr,Ti)-(Al,Zn,Sn,Pb,Bi)-C system

The hypothesized beneficial effect of Zn, Pb, and Bi to form molten IMCs that assist the formation of MAX phase solid solutions led to the SPS densification of starting powder mixtures with the $(Zr_{0.8},Ti_{0.2})_2(Al_{0.2},Zn_{0.2},Sn_{0.2},LBE_{0.4})_{1.05}C_{0.95}$ stoichiometry at 1350 °C (Zn1350), 1450 °C (Zn1450), and 1500 °C (Zn1500). However, the significant amount of (Zr,Ti)C impurities in all Zn*x* ceramics (Figure 3a-c) suggests that the equimolar concentrations of the low-melting-point Zn/Pb/Bi (totaling 60 at.% of the targeted A-site occupancy) had an adverse effect on phase purity. The Rietveld-refined XRD profiles were used to compile a list of calculated d-spacings, 2θ angles, and relative diffraction intensities of the observed MAX phases (SI Tables S8-S11). Once again, a 211-type MAX phase was the dominant phase in all ceramics regardless of synthesis temperature and without detectable decrease in purity as the sintering temperature increased. Therefore, it is assumed that the formation of parasitic (Zr,Ti)C is not associated with the thermal decomposition of the 211 phase but with the exudation of liquified A-metals during material processing by SPS.

Interestingly, the Zn1350 microstructure exhibited extraordinarily large MAX phase platelets with lengths exceeding 100 µm (Figure 3d,e; SI Figure S3), apparently due to the Zn-driven liquid phase formation. Consequently, the ceramic hardness (<3 GPa; Table 2) dropped considerably, increasing the severity of material deformation during Vickers indentation and forming a 'crater-like' surface depression (Figure 3f). Moreover, the majority of MAX phase platelets exhibited a core-rim structure (see compositional contrast in Figure 3e,i), which comprised an “A-element-deficient” core with 312 atomic stacking and an “A-element-rich” rim with 211 atomic stacking. Apart from minor Ti-enrichment, the site-specific elemental compositions (Table 2) did not differ significantly between 312 core and 211 rim, ruling out element-specific diffusion limitations. Instead, atomically resolved STEM (Figure 3g,h) identified a quasi-perfect 312 atomic stacking in the MAX phase grain core with erratic 'bands' made of single layers with the 211 atomic stacking. Moreover, the 312-type MAX phase could be clearly distinguished from its 211-type equivalent, both structurally by XRD (Figure 3a) and visually by SEM/EDS (Figure 3e), confirming its presence in the bulk ceramic. However, the 312-type MAX phase was not detected in Zn1450 & Zn1500, and the corresponding microstructures appeared less coarse (SI Figure S3a,d), with clusters of much smaller MAX phase grains (SI Figure S3b,e). These observations suggest that the formation of the 312-type MAX phase is limited to lower temperatures and is also responsible for accelerated grain growth. Unlike the Pb*x*/LBE*x* ceramics, the combined effect of Zn-induced liquid phase formation and Bi-incorporation on the A-site was required to achieve consistent 312-type MAX phase formation.

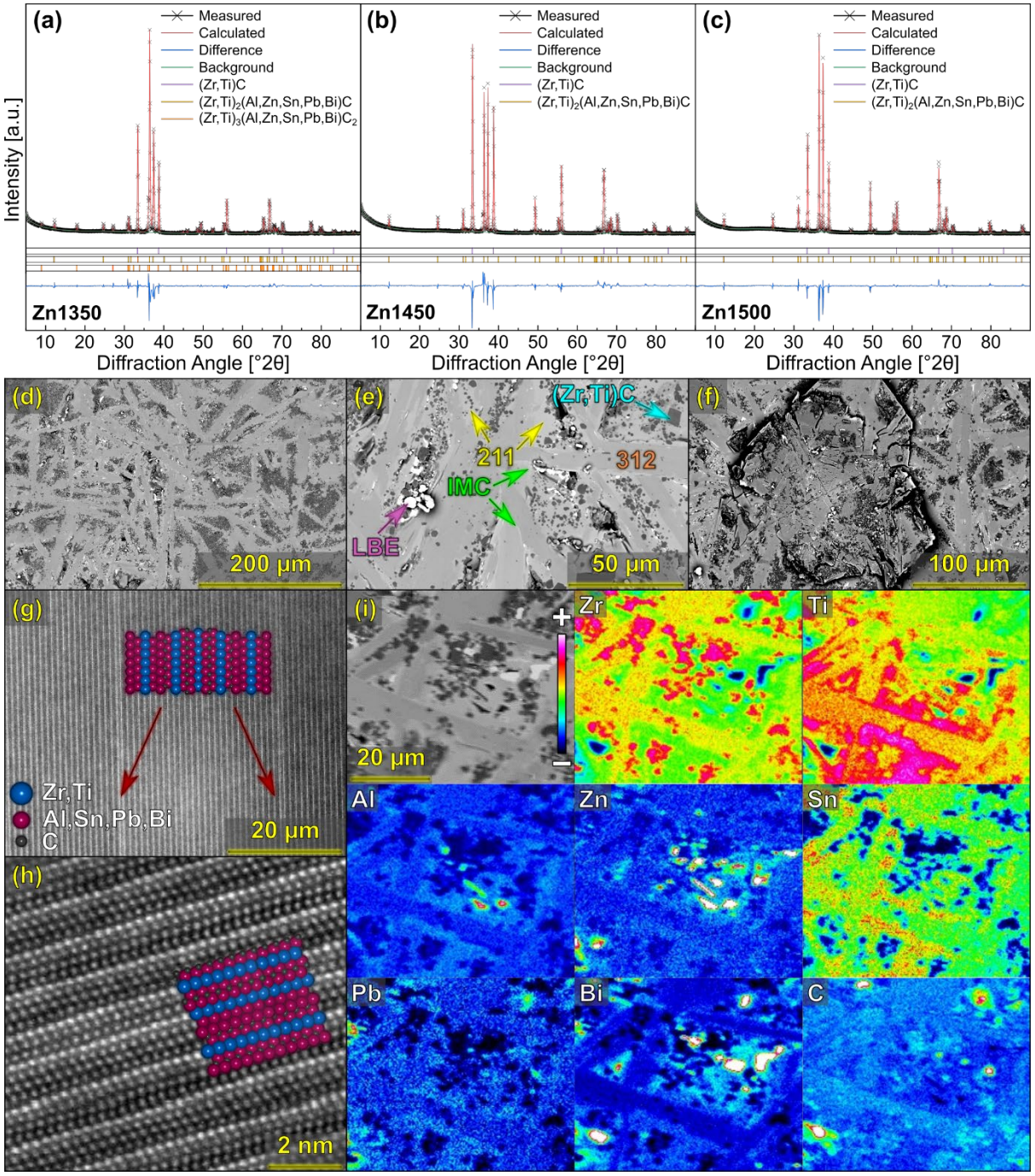

Figure 3. XRD patterns and Rietveld structural refinement of (a) Zn1350, (b) Zn1450, and (c) Zn1500 MAX phase ceramics in the (Zr,Ti)-(Al,Zn,Sn,Pb,Bi)-C system. SEM analysis (BSE, 20 kV) of Zn1350 revealed (d,e) coarse MAX phase platelets with (312 core)/(211 rim) structure; and (f) the formation of a 'crater-like' surface depression near a Vickers indentation. Atomically resolved STEM analysis of Zn1350 showed (g,h) local 211/312 mixed atomic stacking along the *c*-axis ([$11\bar{2}0$] Z.A.; atomic models superimposed). (i) EPMA/WDS elemental mapping confirmed the compositional (312 core)/(211 rim) structure of the coarse MAX phase grains.

The complex formation mechanism of the $(Zr,Ti)_3(Al,Sn,Pb,Bi)C_2$ MAX phase solid solution is best understood by comparing it with the synthesis of the closely related Ti_3SnC_2 and Zr_3SnC_2 ternary compounds, which required the presence of molten IMCs (formed by minute Fe, Co, or Ni additions) for successful reactive sintering according to the following reaction paths:[56, 61]

$$M_2SnC + MC \rightarrow M_3SnC_2 \quad (M = Ti, Zr) \tag{1}$$

$$M_5Sn_3 + 2\,MC + 2\,M + 4\,C \rightarrow 3\,M_3SnC_2 \quad (M = Ti, Zr) \tag{2}$$

Reaction 1 describes the 'conventional' formation path for a 312-type MAX phase through the reaction of the corresponding 211-type MAX phase and binary carbide. The unusually low synthesis temperatures (<1200 °C) reported for Ti_3SnC_2 & Zr_3SnC_2 lead to the hypothesis that 312-type MAX phase formation may result directly from (a) carbide/C & M-element dissolution in the molten IMC, and (b) MAX phase precipitation from the (molten) IMC (Reaction 2).[61] Indeed, Reaction 1 intrinsically fails to account for the crucial role of the liquid phase and has, therefore, been redefined in Reaction 3, specifically for the Zr_3SnC_2 ternary compound:[56]

$$3\,Zr_2SnC + C + (Fe/Co/Ni)_xSn_y^{LIQ} \rightarrow 2\,Zr_3SnC_2 + (Fe/Co/Ni)_xSn_{y+1}^{LIQ} \tag{3}$$

The Fe, Co, and Ni additions promote the formation of a Sn-based liquid phase that (a) enables C dissolution;[62] (b) improves carbide wetting;[63] and (c) allows fast Sn/C diffusion,[64] unlike liquid elemental Sn. In this work, Zn addition appears to have achieved the same outcome by readily alloying with Al,[65] Sn,[66] Pb,[67] and Bi,[68] forming a liquid phase that demonstrated good wetting with the MAX phase and the fine (Zr,Ti)C grains that were co-dispersed along GBs and triple junctions (Figures 1e,3e). Moreover, the A-element gradient (Figure 3i) between the A-deficient 312-type platelet core, the A-enriched 211-type platelet rim, and the A-abundant GB phase exemplifies the outward Sn diffusion suggested in Reaction 3. The absence of atomic stacking anomalies (Figures 1h,3h), such as double A-layers or mixed stackings, distinguished the herein observed structural transition from the related topotactic transformation.[27, 57]

Apart from promoting liquid phase formation, Zn alloying concurrently lowers the boiling point (T_b) of the A-elements close to the synthesis temperatures (e.g., 15 at.% Zn reduces T_b(Pb) from 1749 °C to below 1000 °C under atmospheric pressure)[69]. Indeed, heavy metal-enriched IMC GB phases did not appear in the Zn1450/Zn1500 microstructures (SI Figure S3a,d), with a small Pb content (3.1 at.%, Table 2) being detected by SEM/EDS in Zn1500. Arguably, the vacuum synthesis of the 312-type MAX phase was limited due to volatile A-element losses rather than due to its intrinsic thermal stability.

3.4 Enthalpic & entropic stabilization of chemically complex MAX phase solid solutions

Unit cell distortions are useful indicators of MAX phase (de)stabilization during solid solution formation, quantifying the atomic displacements in the M_6X octahedra (O_d, Equation 4) and M_6A trigonal prisms (P_d, Equation 5). Strongly sterically dissimilar elements (e.g., Zr and Al) strain the MAX phase unit cell and are considered incompatible. Their simultaneous use often correlates with experimental observations of reduced MAX phase stability and low overall phase purity of the produced bulk ceramics. For example, whilst reporting $Zr_2(Al,Bi)C$ solid solution formation, Horlait et al.[48] remarked that "the end members Zr_2BiC and Zr_2AlC seemingly cannot be formed". Therefore, the main goal of solid solution formation is to effectively reduce the overall lattice distortions, O_d and P_d, given by Equations 4 & 5 below:

$$O_d = \frac{\sqrt{3}}{2\sqrt{4z_M^2\left(\frac{c}{a}\right)^2 + \frac{1}{12}}} \tag{4}$$

$$P_d = \frac{1}{\sqrt{\frac{1}{3} + \left(\frac{1}{4} - z_M\right)^2\left(\frac{c}{a}\right)^2}} \tag{5}$$

Table 3 summarizes the calculated MAX phase lattice distortions based on their structural Rietveld refinement (Table 2) or reported lattice parameters. All ceramics comprised MAX phases with consistent distortions in the 1.08-1.10 range, denoting a mild straining of the unit cell with respect to an ideal *hcp* structure that assumes equisized atoms. The synthesis of chemically complex A-site MAX phase solid solutions resulted consistently in the alleviation of the internal strains caused by sterically dissimilar elements (e.g., Sn/Pb in Ti_2SnC, Ti_2PbC, and Zr_2PbC; see Figure 4a) to a larger extent than earlier reported for $Zr_2(Al,Pb,Bi)C$ solid solutions. The intentional occupancy of the M-site predominantly by large Zr atoms was successfully balanced by the preferred occupancy of the A-site by Pb/Bi and especially Sn, illustrating the versatility of Sn as an intermediate-size A-element in complex solid solution design. Moreover, senary $(Zr,Ti)_2(Al,Sn,Pb)C$ (Pb*x*) MAX phase solid solutions appeared consistently less strained (Figure 4b) than the septenary $(Zr,Ti)_2(Al,Sn,Pb,Bi)C$ (LBE*x*/Zn*x*) MAX phase formulations, underscoring the challenging incorporation of large Bi atoms in the produced MAX phases. These observations hold regardless of the exact atomic positions (often not reported or refined; Table 3), which are nonetheless assumed ideal ($z_M = 1/12$) to permit meaningful comparisons.

Table 3. Reported lattice parameters for the MAX phases compared in Figure 4. Entries without refined z_M values appear in *italics* and have been omitted from Figure 4b.

MAX phase compound	a [Å]	c [Å]	z_M	O_d	P_d	Ref.
Ti_2AlC	3.04	13.6	0.086	1.054	1.071	[70]
	3.0593	13.6571	0.0861	1.055	1.073	[71]
	3.06	13.6	0.085	1.071	1.071	[72]
Ti_2SnC	3.1612	13.6763	0.08114	1.141	1.074	[72]
	3.186	13.63	0.086	1.096	1.101	[70]
Ti_2PbC	*3.209*	*13.81*	*1/12*	*1.120*	*1.086*	[73]
Zr_2AlC	3.3237	14.5705	0.0871	1.061	1.089	[24]
Zr_2SnC	3.347	14.59	0.086	1.078	1.088	[70]
Zr_2PbC	*3.384*	*14.667*	*1/12*	*1.113*	*1.081*	[74]
$Ti_2(Al_{0.5},Sn_{0.5})C$	3.1077	13.7105	0.08353	1.094	1.070	[72]
$Zr_2(Al_{0.5},Sn_{0.5})C$	3.344	14.568	0.088	1.057	1.097	[33]
$Zr_2(Al_{0.35},Pb_{0.65})C$	*3.3649*	*14.645*	*1/12*	*1.109*	*1.079*	[43]
$Zr_2(Al_{0.5},Bi_{0.5})C$	*3.344*	*14.51*	*1/12*	*1.112*	*1.081*	[48]
$Zr_2(Al_{0.7},Pb_{0.1},Bi_{0.2})C$	*3.3472*	*14.5401*	*1/12*	*1.111*	*1.080*	[25]
$(Ti_{0.5},Zr_{0.5})_2AlC$	*3.1813*	*14.0204*	*1/12*	*1.097*	*1.070*	[36]
$(Ti_{0.5},Zr_{0.5})_2(Al_{0.5},Sn_{0.5})C$	3.242	14.175	0.084	1.097	1.078	[33]
Pb1350	3.3032	14.4265	0.08499	1.087	1.083	This work
Pb1450	3.3010	14.4201	0.08516	1.085	1.084	This work
Pb1500	3.3058	14.4323	0.08538	1.083	1.085	This work
LBE1350	3.3220	14.4435	0.08538	1.087	1.087	This work
LBE1450	3.3162	14.4317	0.08489	1.092	1.085	This work
LBE1500	3.3194	14.4321	0.08551	1.086	1.088	This work
Zn1350	3.3182	14.4161	0.08555	1.086	1.089	This work
Zn1450	3.3231	14.4493	0.08520	1.089	1.087	This work
Zn1550	3.3181	14.4315	0.08448	1.097	1.084	This work

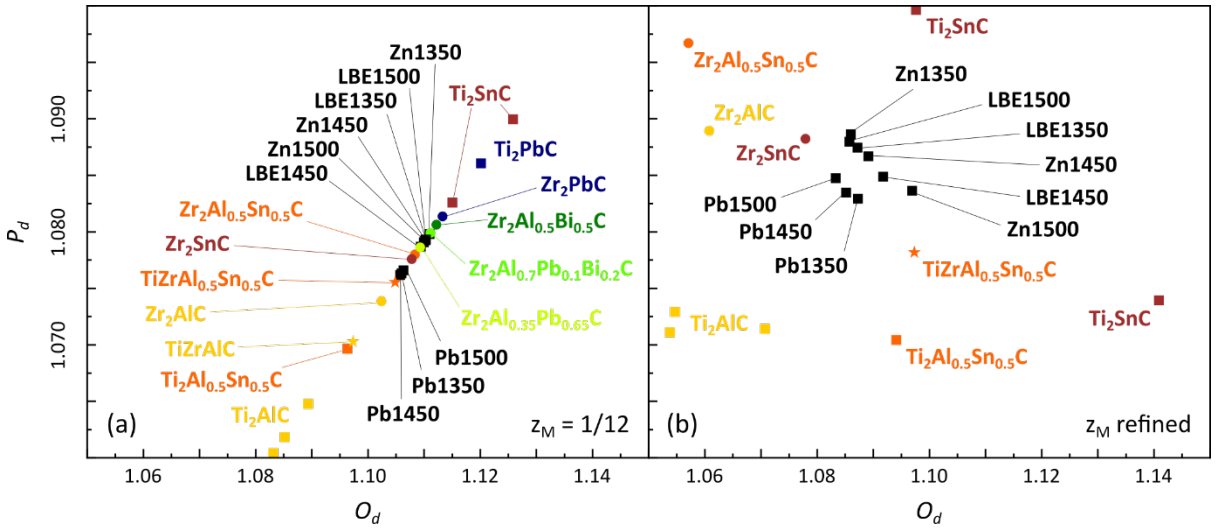

Figure 4. Lattice distortion (P_d, O_d) comparison between compositionally complex MAX phase solid solutions and relevant ternary and simple solid solutions reported in literature (see Table 4). Lattice distortion comparison for (a) the case where the ideal canonical position $z_M = 1/12$ has been assumed for all MAX phases, allowing a fair comparison (linear dependence of P_d on O_d), and (b) the case where only the MAX phases with Rietveld-refined z_M values (see Table 4) are plotted.

Strong discrepancies in the reported structural refinements of the same MAX phase compounds, sometimes encountered in previously published works, occlude confident correlations between lattice distortions and MAX phase stability. For example, even though Ti_2SnC is known to be a stable and easy to process MAX phase, the discrepancies in reported crystallographic data (see Table 3) create confusion whether its unit cell is strongly or mildly distorted, both octahedrally (O_d) and prismatically (P_d) (see Figure 4, where Ti_2SnC appears in a couple of cases as an unexpectedly strong outlier, suggesting an inherent structural instability that has never been experimentally observed and/or reported). It is worth noting that octahedral distortions (O_d) favor the stabilization of the competing (pseudo)binary carbides,[75] whereas prismatic distortions (P_d) are usually associated with difficult to form MAX phases, as confirmed during prior synthesis efforts of ternary MAX phase compounds in the Zr-Al-C and Hf-Al-C systems.[24, 26-28, 31]

Apart from the (enthalpic in nature) crystal structural stabilization, the synthesis of high-purity MAX phase solid solution ceramics benefits from an increased configurational entropy associated with the alloying of one or more sites in the lattice. Conventionally, the configurational entropy of a solid solution (ΔS_{conf}; Equation 6) is maximized for quasi equimolar elemental occupancies (x_i) according to Equation 6, where R is the universal gas constant ($R = 8.314$ J mol^{-1}K^{-1}):

$$\Delta S_{conf} = -R \sum_i x_i \ln x_i \quad (6)$$

Originally defined for alloys with at least 5 major components and $\Delta S_{conf} \geq 1.61R$ (for an equimolar quinary system), 1.5R is often considered as the minimum empirical threshold of a 'high-entropy' system with considerable entropic stabilization.[76, 77] However, the classical high-entropy alloy (HEA) definition cannot be directly transferred to MAX phase crystal lattices in possession of multiple atomic (Wyckoff) sites with independent site occupancies. Therefore, each atomic site will contribute differently to the overall configurational entropy of a MAX phase compound.[78] Equation 7 defines an "entropy metric" (EM), explicitly considering the number of different sublattices (N_{SL}), their sites (a_{SL}), and occupancies ($x_{i,SL}$).[79] EM values exceeding 1.5 indicate 'high-entropy' structures, as follows:

$$\mathrm{EM} = \frac{-N_{SL} \sum_{SL} a_{SL} \sum_i x_{i,SL} \ln x_{i,SL}}{\sum_{SL} a_{SL}} \quad (7)$$

All observed $(Zr,Ti)_2(Al,Sn,Pb)C$ & $(Zr,Ti)_2(Al,Sn,Pb,Bi)C$ MAX phase solid solutions satisfy the EM-based criterion (see Table 4), thus assigning them the denomination "high-entropy". Despite the chemical restrictions imposed on the M-site occupancy and the processing-related A-element losses that can result in strongly non-equimolar elemental occupancies of both M- & A-sites, the total configurational entropy was sufficiently enhanced. Generally, septenary $(2M)_2(4A)_1X_1$ MAX phase solid solutions benefit more from entropic stabilization than senary $(2M)_2(3A)_1X_1$ complex compounds. However, small elemental site occupancies (e.g., 3 at.% Pb in Zn1500) in septenary phases do not contribute significantly to the overall configurational entropy, leading to entropic stabilization comparable to that of senary phases. Even though not every atomic site requires quasi equimolar occupancies (e.g., the M-site in this work), every alloying element should be added in appreciable amounts to the complex MAX phase solid solution. Therefore, MAX phase stabilization via complex solid solution synthesis should not focus on the absolute number of constituent elements, but rather on attaining sterically balanced M- & A-site occupancies by incorporating all constituent elements in non-negligible amounts.

Table 4. Entropy quantifiers of the complex A-site solid solution MAX phases calculated based on SEM/EDS quantified phase compositions (Table 2) excluding Zn.

	ΔS_{conf}^{M}	ΔS_{conf}^{A}	ΔS_{conf}^{X}	a_M	a_A	a_X	N_{SL}	EM
Pb1350	0.573R	0.971R	0	2	1	1	3	1.588
Pb1450	0.581R	0.950R	0	2	1	1	3	1.584
Pb1500	0.560R	0.960R	0	2	1	1	3	1.560
LBE1350	0.521R	1.261R	0	2	1	1	3	1.727
LBE1450	0.527R	1.265R	0	2	1	1	3	1.739
LBE1500	0.534R	1.263R	0	2	1	1	3	1.749
Zn1350	0.532R	1.228R	0	2	1	1	3	1.719
Zn1450	0.531R	1.288R	0	2	1	1	3	1.762
Zn1500	0.502R	1.108R	0	2	1	1	3	1.584

4. Conclusions

Spark plasma densification of powder mixtures in the (Ti,Zr)-(Al,Zn,Sn,Pb,Bi)-C system within the 1350-1500 °C range demonstrated the combined enthalpic and entropic stabilization effect of chemically complex A-site solid solution synthesis as a path to produce high-purity MAX phase bulk ceramics. All ceramics consisted predominantly of 211-type MAX phase solid solutions with varying amounts of (Ti,Zr)C impurity carbides. The addition of metallic Zn or LBE (Pb-Bi eutectic) facilitated the formation of low-melting-point IMCs that promoted elemental diffusion, leading to the development of coarse-grained (20-30 μm in length, 5-10 μm in thickness), soft (3-5 GPa), and damage-resistant ceramics. However, Zn did not occupy the A-site, solely functioning as a sintering aid. When added together, Zn and LBE (Pb/Bi) assisted synergistically the molten IMCs to actively (a) dissolve C, (b) improve Sn/C diffusion, and (c) enable the wetting of (antecedent) (pseudo)binary & ternary carbide phases during SPS densification. Thereby, 211-type MAX phase solid solutions could partially transform into their corresponding 312 counterparts, morphing the microstructure into excessively coarse platelets (lengths ≫100 μm) with a distinct BSE contrast associated with the (312 core)/(211 shell) grain configuration. XRD confirmed 312-type MAX phase formation at 1350 °C, whilst HAADF STEM revealed a sharp intragranular 211-to-312 atomic stacking order transition. Higher SPS synthesis temperatures, however, caused losses of the beneficent Zn-rich phase, inhibiting the transition to the 312-type MAX phase. The strategy of chemically complex MAX phase solid solution synthesis on the A-site resulted in the structural

stabilization of Zr-rich compounds by alleviating lattice distortions caused by sterically dissimilar M- & A-elements, whilst benefitting from configurational entropy stabilization stemming from adequately balanced (relative) M- & A-site occupancies. This work reinforced the hypothesis that the synthesis of chemically complex solid solutions is a powerful design strategy that can be used to produce quasi phase-pure MAX phase ceramics with homogeneous microstructures despite stringent compositional restrictions imposed by the targeted application. This work reiterates the remarkable ability of MAX phase solid solution synthesis to produce ceramics that can meet the needs of the targeted application through precise chemistry tailoring, whilst also putting the ongoing debate over the conditional appropriateness of the term "high-entropy" into perspective.

Supporting Information

1. Full peak indexing of all experimental X-ray diffraction (XRD) patterns (Tables S1-S10).
2. Additional microstructural images (acquired by scanning electron microscopy, SEM, with a backscattered electron, BSE, detector) of all sintered MAX phase ceramics (Figures S1-S3).

Author Information

Corresponding author:

Nick Goossens – *Department of Materials Engineering, KU Leuven, Kasteelpark Arenberg 44, BE-3001 Heverlee, Belgium; Laboratory for High Performance Ceramics, Empa, Überlandstrasse 129, CH-8600, Dübendorf, Switzerland*; *https://orcid.org/0000-0001-5998-2852*; Email: nick.goossens@empa.ch

Authors:

Bensu Tunca – *Department of Materials Engineering, KU Leuven, Kasteelpark Arenberg 44, BE-3001 Heverlee, Belgium; https://orcid.org/0000-0001-8611-3636*

Michael Stuer – *Laboratory for High Performance Ceramics, Empa, Überlandstrasse 129, CH-8600, Dübendorf, Switzerland; https://orcid.org/0002-5937-0626*

Per O.Å. Persson – *Department of Physics, Chemistry, and Biology (IFM), Linköping University, SE-58183, Linköping, Sweden, https://orcid.org/0000-0001-9140-6724*

Jin Won Seo – *Department of Materials Engineering, KU Leuven, Kasteelpark Arenberg 44, BE-3001 Heverlee, Belgium; https://orcid.org/0000-0003-4937-0769*

Shuigen Huang – *Department of Materials Engineering, KU Leuven, Kasteelpark Arenberg 44, BE-3001 Heverlee, Belgium; https://orcid.org/0000-0002-9401-6921*

Konstantina Lambrinou – *School of Computing and Engineering, University of Huddersfield, Queensgate, Huddersfield HD1 3DH, United Kingdom; https://orcid.org/0000-0002-1264-6699*

Jozef Vleugels – *Department of Materials Engineering, KU Leuven, Kasteelpark Arenberg 44, BE-3001 Heverlee, Belgium; https://orcid.org/0000-0003-4432-4675*

Notes

The authors declare no competing financial interest.

Acknowledgements

N.G. thanks the Fund for Scientific Research Flanders (FWO-Vlaanderen) for his PhD-related fundamental research fellowship No 1118120N. Zahid Anwer (KU Leuven) and Innocent Ehikhioya (University of Huddersfield) are acknowledged for FIB milling the thin films subjected to TEM analysis. SCK CEN (Belgian Nuclear Research Centre) is gratefully acknowledged for providing a block of solid LBE for MAX phase solid solution synthesis. The authors acknowledge the Swedish Research Council (VR) and the Swedish Foundation for Strategic Research (SSF) for access to ARTEMI, the Swedish National Infrastructure in Advanced Electron Microscopy (2021-00171 and RIF21-0026). J.W.S. acknowledges the FWO Infrastructure projects AKUL/13/19 and I000920N. The authors also acknowledge financial support from the Euratom research and training programme 2014-2018 under Grant Agreement No 740415 (H2020 IL TROVATORE).

References

(1) Barsoum, M. W. *MAX Phases: Properties of Machinable Ternary Carbides and Nitrides*; Wiley-VCH Verlag GmbH & Co. KGaA, 2013. DOI: 10.1002/9783527654581.
(2) Gonzalez-Julian, J. Processing of MAX phases: From synthesis to applications. *Journal of the American Ceramic Society* **2021**, *104* (2), 659-690. DOI: 10.1111/jace.17544.
(3) Goossens, N.; Tunca, B.; Lapauw, T.; Lambrinou, K.; Vleugels, J. MAX Phases, Structure, Processing, and Properties. In *Encyclopedia of Materials: Technical Ceramics and Glasses*, Pomeroy, M. Ed.; Elsevier, 2021; pp 182-199.
(4) Bonk, A.; Sau, S.; Uranga, N.; Hernaiz, M.; Bauer, T. Advanced heat transfer fluids for direct molten salt line-focusing CSP plants. *Progress in Energy and Combustion Science* **2018**, *67*, 69-87. DOI: 10.1016/j.pecs.2018.02.002.
(5) Walczak, M.; Pineda, F.; Fernández, Á. G.; Mata-Torres, C.; Escobar, R. A. Materials corrosion for thermal energy storage systems in concentrated solar power plants. *Renewable and Sustainable Energy Reviews* **2018**, *86*, 22-44. DOI: 10.1016/j.rser.2018.01.010.
(6) Van Loo, K.; Lapauw, T.; Ozalp, N.; Ström, E.; Lambrinou, K.; Vleugels, J. Compatibility of SiC- and MAX phase-based ceramics with a KNO_3-$NaNO_3$ molten solar salt. *Solar Energy Materials and Solar Cells* **2019**, *195*, 228-240. DOI: 10.1016/j.solmat.2019.03.007.

(7) Azina, C.; Badie, S.; Litnovsky, A.; Silvestroni, L.; Sani, E.; Gonzalez-Julian, J. Optical properties and corrosion resistance of Ti_2AlC, Ti_3AlC_2, and Cr_2AlC as candidates for concentrated solar power receivers. *Solar Energy Materials and Solar Cells* **2023**, *259*, 112433. DOI: 10.1016/j.solmat.2023.112433.
(8) Nuttin, A.; Heuer, D.; Billebaud, A.; Brissot, R.; Le Brun, C.; Liatard, E.; Loiseaux, J. M.; Mathieu, L.; Meplan, O.; Merle-Lucotte, E.; et al. Potential of thorium molten salt reactors, detailed calculations and concept evolution with a view to large scale energy production. *Progress in Nuclear Energy* **2005**, *46* (1), 77-99. DOI: 10.1016/j.pnucene.2004.11.001.
(9) Lambrinou, K.; Charalampopoulou, E.; Van Der Donck, T.; Delville, R.; Schryvers, D. Dissolution corrosion of 316L austenitic stainless steels in contact with static liquid lead-bismuth eutectic (LBE) at 500 °C. *Journal of Nuclear Materials* **2017**, *490*, 9-27. DOI: 10.1016/j.jnucmat.2017.04.004.
(10) Charalampopoulou, E.; Lambrinou, K.; Van Der Donck, T.; Paladino, B.; Di Fonzo, F.; Azina, C.; Eklund, P.; Mráz, S.; Schneider, J. M.; Schryvers, D.; et al. Early stages of dissolution corrosion in 316L and DIN 1.4970 austenitic stainless steels with and without anticorrosion coatings in static liquid lead-bismuth eutectic (LBE) at 500 °C. *Materials Characterization* **2021**, *178*, 111234. DOI: 10.1016/j.matchar.2021.111234.
(11) Gong, X.; Short, M. P.; Auger, T.; Charalampopoulou, E.; Lambrinou, K. Environmental degradation of structural materials in liquid lead- and lead-bismuth eutectic-cooled reactors. *Progress in Materials Science* **2022**, *126*, 100920. DOI: 10.1016/j.pmatsci.2022.100920.
(12) Lapauw, T.; Tunca, B.; Joris, J.; Jianu, A.; Fetzer, R.; Weisenburger, A.; Vleugels, J.; Lambrinou, K. Interaction of $M_{n+1}AX_n$ phases with oxygen-poor, static and fast-flowing liquid lead-bismuth eutectic. *Journal of Nuclear Materials* **2019**, *520*, 258-272. DOI: 10.1016/j.jnucmat.2019.04.010.
(13) Heinzel, A.; Müller, G.; Weisenburger, A. Compatibility of Ti_3SiC_2 with liquid Pb and PbBi containing oxygen. *Journal of Nuclear Materials* **2009**, *392* (2), 255-258. DOI: 10.1016/j.jnucmat.2009.03.004.
(14) Heinzel, A.; Weisenburger, A.; Müller, G. Long-term corrosion tests of Ti_3SiC_2 and Ti_2AlC in oxygen containing LBE at temperatures up to 700 °C. *Journal of Nuclear Materials* **2016**, *482*, 114-123. DOI: 10.1016/j.jnucmat.2016.10.007.
(15) Whittle, K. R.; Blackford, M. G.; Aughterson, R. D.; Moricca, S.; Lumpkin, G. R.; Riley, D. P.; Zaluzec, N. J. Radiation tolerance of $M_{n+1}AX_n$ phases, Ti_3AlC_2 and Ti_3SiC_2. *Acta Materialia* **2010**, *58* (13), 4362-4368. DOI: 10.1016/j.actamat.2010.04.029.
(16) Tallman, D. J.; He, L.; Gan, J.; Caspi, E. a. N.; Hoffman, E. N.; Barsoum, M. W. Effects of neutron irradiation of Ti_3SiC_2 and Ti_3AlC_2 in the 121–1085 °C temperature range. *Journal of Nuclear Materials* **2017**, *484*, 120-134. DOI: 10.1016/j.jnucmat.2016.11.016.
(17) Tallman, D. J.; He, L.; Garcia-Diaz, B. L.; Hoffman, E. N.; Kohse, G.; Sindelar, R. L.; Barsoum, M. W. Effect of neutron irradiation on defect evolution in Ti_3SiC_2 and Ti_2AlC. *Journal of Nuclear Materials* **2016**, *468*, 194-206. DOI: 10.1016/j.jnucmat.2015.10.030.
(18) Ang, C.; Parish, C. M.; Shih, C.; Silva, C.; Katoh, Y. Microstructure and mechanical properties of titanium aluminum carbides neutron irradiated at 400–700°C. *Journal of the European Ceramic Society* **2017**, *37* (6), 2353-2363. DOI: 10.1016/j.jeurceramsoc.2017.01.024.
(19) Ang, C.; Silva, C.; Shih, C.; Koyanagi, T.; Katoh, Y.; Zinkle, S. J. Anisotropic swelling and microcracking of neutron irradiated Ti_3AlC_2–$Ti_5Al_2C_3$ materials. *Scripta Materialia* **2016**, *114*, 74-78. DOI: 10.1016/j.scriptamat.2015.11.008.
(20) Clark, D. W.; Zinkle, S. J.; Patel, M. K.; Parish, C. M. High temperature ion irradiation effects in MAX phase ceramics. *Acta Materialia* **2016**, *105*, 130-146. DOI: 10.1016/j.actamat.2015.11.055.
(21) Lunt, D.; Thomas, R.; Bowden, D.; Rigby-Bell, M. T. P.; Shubeita, S. d. M.; Andrews, C.; Lapauw, T.; Vleugels, J.; da Fonseca, J. Q.; Lambrinou, K.; et al. Detecting irradiation-induced strain localisation on the microstructural level by means of high-resolution digital image correlation. *Journal of Nuclear Materials* **2023**, *580*, 154410. DOI: 10.1016/j.jnucmat.2023.154410.
(22) Patel, M. K.; Tallman, D. J.; Valdez, J. A.; Aguiar, J.; Anderoglu, O.; Tang, M.; Griggs, J.; Fu, E.; Wang, Y.; Barsoum, M. W. Effect of helium irradiation on Ti_3AlC_2 at 500°C. *Scripta Materialia* **2014**, *77*, 1-4. DOI: 10.1016/j.scriptamat.2013.12.010.

(23) Tunca, B.; Greaves, G.; Hinks, J. A.; Persson, P. O. Å.; Vleugels, J.; Lambrinou, K. In situ He^+ irradiation of the double solid solution $(Ti_{0.5},Zr_{0.5})_2(Al_{0.5},Sn_{0.5})C$ MAX phase: Defect evolution in the 350–800 °C temperature range. *Acta Materialia* **2021**, *206*, 116606. DOI: 10.1016/j.actamat.2020.116606.
(24) Lapauw, T.; Lambrinou, K.; Cabioc'h, T.; Halim, J.; Lu, J.; Pesach, A.; Rivin, O.; Ozeri, O.; Caspi, E. N.; Hultman, L.; et al. Synthesis of the new MAX phase Zr_2AlC. *Journal of the European Ceramic Society* **2016**, *36* (8), 1847-1853. DOI: 10.1016/j.jeurceramsoc.2016.02.044.
(25) Tunca, B.; Lapauw, T.; Callaert, C.; Hadermann, J.; Delville, R.; Caspi, E. A. N.; Dahlqvist, M.; Rosén, J.; Marshal, A.; Pradeep, K. G.; et al. Compatibility of Zr_2AlC MAX phase-based ceramics with oxygen-poor, static liquid lead–bismuth eutectic. *Corrosion Science* **2020**, *171*, 108704. DOI: 10.1016/j.corsci.2020.108704.
(26) Lapauw, T.; Halim, J.; Lu, J.; Cabioc'h, T.; Hultman, L.; Barsoum, M. W.; Lambrinou, K.; Vleugels, J. Synthesis of the novel Zr_3AlC_2 MAX phase. *Journal of the European Ceramic Society* **2016**, *36* (3), 943-947. DOI: 10.1016/j.jeurceramsoc.2015.10.011.
(27) Goossens, N.; Tunca, B.; Lambrinou, K.; Vleugels, J. Topotactic transformations in Hf-Al-C MAX phase compounds: Synthesis and characterization of nanolaminated Hf_2AlC, Hf_3AlC_2 and $Hf_5Al_2C_3$. *Open Ceramics* **2024**, *18*, 100584. DOI: 10.1016/j.oceram.2024.100584.
(28) Lapauw, T.; Tunca, B.; Cabioc'h, T.; Lu, J.; Persson, P. O. Å.; Lambrinou, K.; Vleugels, J. Synthesis of MAX Phases in the Hf–Al–C System. *Inorganic Chemistry* **2016**, *55* (21), 10922-10927. DOI: 10.1021/acs.inorgchem.6b01398.
(29) Qarra, H. H.; Knowles, K. M.; Vickers, M. E.; Akhmadaliev, S.; Lambrinou, K. Heavy ion irradiation damage in Zr_2AlC MAX phase. *Journal of Nuclear Materials* **2019**, *523*, 1-9. DOI: 10.1016/j.jnucmat.2019.05.034.
(30) Goossens, N.; Lapauw, T.; Lambrinou, K.; Vleugels, J. Synthesis of MAX phase-based ceramics from early transition metal hydride powders. *Journal of the European Ceramic Society* **2022**, *42* (16), 7389-7402. DOI: 10.1016/j.jeurceramsoc.2022.09.025.
(31) Lapauw, T.; Tunca, B.; Potashnikov, D.; Pesach, A.; Ozeri, O.; Vleugels, J.; Lambrinou, K. The double solid solution $(Zr,Nb)_2(Al,Sn)C$ MAX phase: a steric stability approach. *Scientific Reports* **2018**, *8* (1). DOI: 10.1038/s41598-018-31271-2.
(32) Tunca, B.; Huang, S.; Goossens, N.; Lambrinou, K.; Vleugels, J. Chemically complex double solid solution MAX phase-based ceramics in the (Ti,Zr,Hf,V,Nb)-(Al,Sn)-C system. *Materials Research Letters* **2022**, *10* (2), 52-61. DOI: 10.1080/21663831.2021.2017043.
(33) Tunca, B.; Lapauw, T.; Delville, R.; Neuville, D. R.; Hennet, L.; Thiaudière, D.; Ouisse, T.; Hadermann, J.; Vleugels, J.; Lambrinou, K. Synthesis and Characterization of Double Solid Solution $(Zr,Ti)_2(Al,Sn)C$ MAX Phase Ceramics. *Inorganic Chemistry* **2019**, *58* (10), 6669-6683. DOI: 10.1021/acs.inorgchem.9b00065.
(34) Bowden, D.; Ward, J.; Middleburgh, S.; de Moraes Shubeita, S.; Zapata-Solvas, E.; Lapauw, T.; Vleugels, J.; Lambrinou, K.; Lee, W. E.; Preuss, M.; et al. The stability of irradiation-induced defects in Zr_3AlC_2, Nb_4AlC_3 and $(Zr_{0.5},Ti_{0.5})_3AlC_2$ MAX phase-based ceramics. *Acta Materialia* **2020**, *183*, 24-35. DOI: 10.1016/j.actamat.2019.10.049.
(35) Lapauw, T.; Tytko, D.; Vanmeensel, K.; Huang, S.; Choi, P.-P.; Raabe, D.; Caspi, E. a. N.; Ozeri, O.; to Baben, M.; Schneider, J. M.; et al. $(Nb_x,Zr_{1-x})_4AlC_3$ MAX Phase Solid Solutions: Processing, Mechanical Properties, and Density Functional Theory Calculations. *Inorganic Chemistry* **2016**, *55* (11), 5445-5452. DOI: 10.1021/acs.inorgchem.6b00484.
(36) Tunca, B.; Lapauw, T.; Karakulina, O. M.; Batuk, M.; Cabioc'h, T.; Hadermann, J.; Delville, R.; Lambrinou, K.; Vleugels, J. Synthesis of MAX Phases in the Zr-Ti-Al-C System. *Inorganic Chemistry* **2017**, *56* (6), 3489-3498. DOI: 10.1021/acs.inorgchem.6b03057.
(37) Ali, M. A.; Hossain, M. M.; Hossain, M. A.; Nasir, M. T.; Uddin, M. M.; Hasan, M. Z.; Islam, A. K. M. A.; Naqib, S. H. Recently synthesized $(Zr_{1-x}Ti_x)_2AlC$ $(0 \le x \le 1)$ solid solutions: Theoretical study of the effects of M mixing on physical properties. *Journal of Alloys and Compounds* **2018**, *743*, 146-154. DOI: 10.1016/j.jallcom.2018.01.396.
(38) Ali, M. A.; Hossain, M. M.; Jahan, N.; Islam, A. K. M. A.; Naqib, S. H. Newly synthesized Zr_2AlC, $Zr_2(Al_{0.58}Bi_{0.42})C$, $Zr_2(Al_{0.2}Sn_{0.8})C$, and $Zr_2(Al_{0.3}Sb_{0.7})C$ MAX phases: A DFT based first-principles

study. *Computational Materials Science* **2017**, *131*, 139-145. DOI: 10.1016/j.commatsci.2017.01.048.
(39) Kale, S.; Tarasov, I.; Driggers, L.; Elliott, L.-L.; Bhatt, P.; Schlueter, C.; Michałowski, P. P.; Rosen, J.; Dahlqvist, M.; Regoutz, A.; et al. Screening of 3d metals as A-elements in MAX phase Nb_2SnC and their effects on the magnetic properties of the solid solutions of $Nb_2(Sn_{1-x}A_x)C$. *Journal of Materials Chemistry C* **2025**. DOI: 10.1039/d5tc02347e.
(40) Bouhemadou, A. Prediction study of structural and elastic properties under pressure effect of M_2SnC (M=Ti, Zr, Nb, Hf). *Physica B: Condensed Matter* **2008**, *403* (17), 2707-2713. DOI: 10.1016/j.physb.2008.02.014.
(41) Dahlqvist, M.; Rosen, J. The rise of MAX phase alloys – large-scale theoretical screening for the prediction of chemical order and disorder. *Nanoscale* **2022**, *14* (30), 10958-10971. DOI: 10.1039/d2nr02414d.
(42) Roncaglia, C.; Lopes, F.; Goossens, N.; Stuer, M.; Passerone, D. Machine Learning Lattice Parameters of M_2AX Phases. *The Journal of Physical Chemistry C* **2025**, *129* (14), 7052-7062. DOI: 10.1021/acs.jpcc.4c08730.
(43) Horlait, D.; Grasso, S.; Chroneos, A.; Lee, W. E. Attempts to synthesise quaternary MAX phases $(Zr,M)_2AlC$ and $Zr_2(Al,A)C$ as a way to approach Zr_2AlC. *Materials Research Letters* **2016**, *4* (3), 137-144. DOI: 10.1080/21663831.2016.1143053.
(44) Sarker, P.; Harrington, T.; Toher, C.; Oses, C.; Samiee, M.; Maria, J.-P.; Brenner, D. W.; Vecchio, K. S.; Curtarolo, S. High-entropy high-hardness metal carbides discovered by entropy descriptors. *Nature Communications* **2018**, *9* (1). DOI: 10.1038/s41467-018-07160-7.
(45) Castle, E.; Csanádi, T.; Grasso, S.; Dusza, J.; Reece, M. Processing and Properties of High-Entropy Ultra-High Temperature Carbides. *Scientific Reports* **2018**, *8* (1). DOI: 10.1038/s41598-018-26827-1.
(46) Gao, H.; Benitez, R.; Son, W.; Arroyave, R.; Radovic, M. Structural, physical and mechanical properties of $Ti_3(Al_{1-x}Si_x)C_2$ solid solution with x=0–1. *Materials Science and Engineering: A* **2016**, *676*, 197-208. DOI: 10.1016/j.msea.2016.08.098.
(47) Cabioch, T.; Eklund, P.; Mauchamp, V.; Jaouen, M.; Barsoum, M. W. Tailoring of the thermal expansion of $Cr_2(Al_x,Ge_{1-x})C$ phases. *Journal of the European Ceramic Society* **2013**, *33* (4), 897-904. DOI: 10.1016/j.jeurceramsoc.2012.10.008.
(48) Horlait, D.; Middleburgh, S. C.; Chroneos, A.; Lee, W. E. Synthesis and DFT investigation of new bismuth-containing MAX phases. *Scientific Reports* **2016**, *6* (1), 18829. DOI: 10.1038/srep18829.
(49) Etzkorn, J.; Ade, M.; Kotzott, D.; Kleczek, M.; Hillebrecht, H. Ti_2GaC, Ti_4GaC_3 and Cr_2GaC—Synthesis, crystal growth and structure analysis of Ga-containing MAX-phases $M_{n+1}GaC_n$ with M=Ti, Cr and n=1, 3. *Journal of Solid State Chemistry* **2009**, *182* (5), 995-1002. DOI: 10.1016/j.jssc.2009.01.003.
(50) Tian, Z.; Yan, B.; Wu, F.; Tang, J.; Xu, X.; Liu, J.; Zhang, P.; Sun, Z. Synthesis of $Ti_2(In_xAl_{1-x})C$ (x = 0–1) solid solutions with high-purity and their properties. *Journal of the European Ceramic Society* **2023**, *43* (14), 5915-5924. DOI: 10.1016/j.jeurceramsoc.2023.06.060.
(51) El-Raghy, T.; Chakraborty, S.; Barsoum, M. W. Synthesis and characterization of Hf_2PbC, Zr_2PbC and M_2SnC (M=Ti, Hf, Nb or Zr). *Journal of the European Ceramic Society* **2000**, *20* (14), 2619-2625. DOI: 10.1016/S0955-2219(00)00127-8.
(52) Zhang, Q.; Wen, B.; Luo, J.; Zhou, Y.; San, X.; Bao, Y.; Chu, L.; Feng, Q.; Grasso, S.; Hu, C. Synthesis of new lead-containing MAX phases of Zr_3PbC_2 and Hf_3PbC_2. *Journal of the American Ceramic Society* **2023**, *106* (11), 6390-6397. DOI: 10.1111/jace.19332.
(53) Ding, H.; Li, Y.; Li, M.; Chen, K.; Liang, K.; Chen, G.; Lu, J.; Palisaitis, J.; Persson, P. O. Å.; Eklund, P.; et al. Chemical scissor–mediated structural editing of layered transition metal carbides. *Science* **2023**, *379* (6637), 1130-1135. DOI: 10.1126/science.add5901.
(54) Ding, H.; Li, Y.; Lu, J.; Luo, K.; Chen, K.; Li, M.; Persson, P. O. Å.; Hultman, L.; Eklund, P.; Du, S.; et al. Synthesis of MAX phases Nb_2CuC and $Ti_2(Al_{0.1}Cu_{0.9})N$ by A-site replacement reaction in molten salts. *Materials Research Letters* **2019**, *7* (12), 510-516. DOI: 10.1080/21663831.2019.1672822.

(55) Li, M.; Lu, J.; Luo, K.; Li, Y.; Chang, K.; Chen, K.; Zhou, J.; Rosen, J.; Hultman, L.; Eklund, P.; et al. Element Replacement Approach by Reaction with Lewis Acidic Molten Salts to Synthesize Nanolaminated MAX Phases and MXenes. *Journal of the American Chemical Society* **2019**, *141* (11), 4730-4737. DOI: 10.1021/jacs.9b00574.
(56) Lapauw, T.; Tunca, B.; Cabioc'h, T.; Vleugels, J.; Lambrinou, K. Reactive spark plasma sintering of Ti_3SnC_2, Zr_3SnC_2 and Hf_3SnC_2 using Fe, Co or Ni additives. *Journal of the European Ceramic Society* **2017**, *37* (15), 4539-4545. DOI: 10.1016/j.jeurceramsoc.2017.06.041.
(57) Lane, N. J.; Naguib, M.; Lu, J.; Hultman, L.; Barsoum, M. W. Structure of a new bulk $Ti_5Al_2C_3$ MAX phase produced by the topotactic transformation of Ti_2AlC. *Journal of the European Ceramic Society* **2012**, *32* (12), 3485-3491. DOI: 10.1016/j.jeurceramsoc.2012.03.035.
(58) Hosemann, P.; Frazer, D.; Stergar, E.; Lambrinou, K. Twin boundary-accelerated ferritization of austenitic stainless steels in liquid lead–bismuth eutectic. *Scripta Materialia* **2016**, *118*, 37-40. DOI: 10.1016/j.scriptamat.2016.02.029.
(59) Glasbrenner, H.; Gröschel, F.; Grimmer, H.; Patorski, J.; Rohde, M. Expansion of solidified lead bismuth eutectic. *Journal of Nuclear Materials* **2005**, *343* (1), 341-348. DOI: 10.1016/j.jnucmat.2004.09.075.
(60) Koseva, R.; Mönch, I.; Meier, D.; Schumann, J.; Arndt, K. F.; Schultz, L.; Zhao, B.; Schmidt, O. G. Evolution of hillocks in Bi thin films and their removal upon nanoscale mechanical polishing. *Thin Solid Films* **2012**, *520* (17), 5589-5592. DOI: 10.1016/j.tsf.2012.04.040.
(61) Ouabadi, N.; Gauthier-Brunet, V.; Cabioc'h, T.; Bei, G. P.; Dubois, S. Formation Mechanisms of Ti_3SnC_2 Nanolaminate Carbide Using Fe as Additive. *Journal of the American Ceramic Society* **2013**, *96* (10), 3239-3242. DOI: 10.1111/jace.12427.
(62) Oden, L. L.; Gokcen, N. A. Sn-C and Al-Sn-C phase diagrams and thermodynamic properties of C in the alloys: 1550 °C to 2300 °C. *Metallurgical Transactions B* **1993**, *24* (1), 53-58. DOI: 10.1007/bf02657871.
(63) Frage, N.; Froumin, N.; Dariel, M. P. Wetting of TiC by non-reactive liquid metals. *Acta Materialia* **2002**, *50* (2), 237-245. DOI: 10.1016/S1359-6454(01)00349-4.
(64) LeClaire, A. D. Diffusion of C, N, and O in metals. In *Diffusion in Solid Metals and Alloys*, Mehrer, H. Ed.; Landolt-Börnstein Group III - Condensed Matter, Vol. 26; Springer-Verlag Berlin Heidelberg, 1990.
(65) Okamoto, H. Al-Zn (aluminum-zinc). *Journal of Phase Equilibria* **1995**, *16* (3), 281-282. DOI: 10.1007/bf02667316.
(66) Moser, Z.; Dutkiewicz, J.; Gasior, W.; Salawa, J. The Sn–Zn (Tin-Zinc) system. *Bulletin of Alloy Phase Diagrams* **1985**, *6* (4), 330-334. DOI: 10.1007/bf02880511.
(67) Hurtado, I.; Jantzen, T.; Spencer, P. J. Thermodynamic description of the stable Pb-Sn-Zn and the metastable Al-Cu-Mg miscibility gaps. *Berichte der Bunsengesellschaft für physikalische Chemie* **1998**, *102* (9), 1088-1094. DOI: 10.1002/bbpc.19981020905.
(68) Vizdal, J.; Braga, M. H.; Kroupa, A.; Richter, K. W.; Soares, D.; Malheiros, L. F.; Ferreira, J. Thermodynamic assessment of the Bi–Sn–Zn System. *Calphad* **2007**, *31* (4), 438-448. DOI: 10.1016/j.calphad.2007.05.002.
(69) Okamoto, H. Pb-Zn (Lead-Zinc). *Journal of Phase Equilibria* **2003**, *24* (5), 482-483. DOI: 10.1361/105497103770330244.
(70) Jeitschko, W.; Nowotny, H.; Benesovsky, F. Kohlenstoffhaltige ternäre Verbindungen (H-Phase). *Monatshefte für Chemie* **1963**, *94* (4), 672-676. DOI: 10.1007/bf00913068.
(71) Hug, G.; Jaouen, M.; Barsoum, M. W. X-ray absorption spectroscopy, EELS, and full-potential augmented plane wave study of the electronic structure of Ti_2AlC, Ti_2AlN, Nb_2AlC, and $(Ti_{0.5}Nb_{0.5})_2AlC$. *Physical Review B* **2005**, *71* (2), 024105. DOI: 10.1103/PhysRevB.71.024105.
(72) Tian, Z.; Zhang, P.; Sun, W.; Yan, B.; Sun, Z. Vegard's law deviating $Ti_2(Sn_xAl_{1-x})C$ solid solution with enhanced properties. *Journal of Advanced Ceramics* **2023**, *12* (8), 1655-1669. DOI: 10.26599/jac.2023.9220779.
(73) Jeitschko, W.; Nowotny, H.; Benesovsky, F. Die H-Phasen Ti_2TlC, Ti_2PbC, Nb_2InC, Nb_2SnC und Ta_2GaC. *Monatshefte für Chemie* **1964**, *95* (2), 431-435. DOI: 10.1007/bf00901306.

(74) Nowotny, V. H. Strukturchemie einiger Verbindungen der Übergangsmetalle mit den elementen C, Si, Ge, Sn. *Progress in Solid State Chemistry* **1971**, *5*, 27-70. DOI: 10.1016/0079-6786(71)90016-1.
(75) Zhao, S. Lattice distortion in high-entropy carbide ceramics from first-principles calculations. *Journal of the American Ceramic Society* **2021**, *104* (4), 1874-1886. DOI: 10.1111/jace.17600.
(76) Sarkar, A.; Wang, Q.; Schiele, A.; Chellali, M. R.; Bhattacharya, S. S.; Wang, D.; Brezesinski, T.; Hahn, H.; Velasco, L.; Breitung, B. High-Entropy Oxides: Fundamental Aspects and Electrochemical Properties. *Advanced Materials* **2019**, *31* (26), 1806236. DOI: 10.1002/adma.201806236.
(77) Yeh, J. W.; Chen, Y. L.; Lin, S. J.; Chen, S. K. High-Entropy Alloys – A New Era of Exploitation. *Materials Science Forum* **2007**, *560*, 1-9. DOI: 10.4028/www.scientific.net/msf.560.1.
(78) Schneider, J. M. How high is the entropy in high entropy ceramics? *Journal of Applied Physics* **2021**, *130* (15), 150903. DOI: 10.1063/5.0062523.
(79) Dippo, O. F.; Vecchio, K. S. A universal configurational entropy metric for high-entropy materials. *Scripta Materialia* **2021**, *201*, 113974. DOI: 10.1016/j.scriptamat.2021.113974.

Supporting Information

Sterically stabilized (Zr,Ti)-(Al,Sn,Pb,Bi)-C MAX phase solid solutions with Zn additions and enhanced chemical complexity on the A-site

Nick Goossens[a,b*], Bensu Tunca[a], Michael Stuer[b], Per O.Å. Persson[c], Jin Won Seo[a], Shuigen Huang[a], Konstantina Lambrinou[d], Jozef Vleugels[a]

[a] *Department of Materials Engineering, KU Leuven, Kasteelpark Arenberg 44, BE-3001 Heverlee, Belgium*

[b] *Laboratory for High Performance Ceramics, Empa, Überlandstrasse 129, CH-8600, Dübendorf, Switzerland*

[c] *Department of Physics, Chemistry, and Biology (IFM), Linköping University, SE-58183, Linköping, Sweden*

[d] *School of Computing and Engineering, University of Huddersfield, Queensgate, Huddersfield HD1 3DH, United Kingdom*

Table S1. The d-spacings, 2θ angles, and relative intensities of all (*hkl*) reflections based on the individual Rietveld-refined diffraction profiles of $(Zr,Ti)_2(Al,Sn,Pb)C$ in Pb1350.

(*hkl*)	d [Å]	$2\theta_{calc}$ [°]	$2\theta_{exp}$ [°]	I/I_{max} [%]
002	7.2133	12.26	12.27	0.30
004	3.6066	24.66	24.69	0.56
100	2.8607	31.24	31.27	21.38
101	2.8060	31.87	31.89	0.70
102	2.6592	33.68	33.71	1.14
103	2.4586	36.52	36.55	100.00
006	2.4044	37.37	37.40	19.23
104	2.2413	40.20	40.24	0.03
105	2.0315	44.57	44.61	0.64
106	1.8406	49.48	49.52	15.72
008	1.8033	50.57	50.62	0.21
107	1.6722	54.86	54.91	0.06
110	1.6516	55.60	55.65	20.63
112	1.6100	57.17	57.22	0.14
108	1.5255	60.66	60.71	0.04
114	1.5016	61.72	61.78	0.23
0010	1.4427	64.55	64.61	0.00
200	1.4303	65.17	65.23	2.63
201	1.4234	65.53	65.59	0.11
202	1.4030	66.60	66.66	0.13
109	1.3984	66.85	66.91	16.42
203	1.3710	68.37	68.43	15.42
116	1.3614	68.92	68.99	18.89
204	1.3296	70.81	70.88	0.00
1010	1.2881	73.45	73.53	0.03
205	1.2815	73.90	73.97	0.16
206	1.2293	77.60	77.68	4.02
118	1.2180	78.46	78.54	0.35
0012	1.2022	79.69	79.77	2.35
1011	1.1922	80.50	80.58	0.21
207	1.1751	81.92	82.00	0.02
208	1.1206	86.85	86.94	0.02
1012	1.1083	88.06	88.15	2.38

Table S2. The d-spacings, 2θ angles, and relative intensities of all (*hkl*) reflections based on the individual Rietveld-refined diffraction profiles of $(Zr,Ti)_2(Al,Sn,Pb)C$ in Pb1450.

(*hkl*)	d [Å]	$2\theta_{calc}$ [°]	$2\theta_{exp}$ [°]	I/I_{max} [%]
002	7.2101	12.27	12.28	0.25
004	3.6050	24.68	24.70	0.54
100	2.8587	31.26	31.29	21.18
101	2.8041	31.89	31.92	0.63
102	2.6575	33.70	33.73	1.19
103	2.4570	36.54	36.57	100.00
006	2.4034	37.39	37.42	19.13
104	2.2399	40.23	40.26	0.04
105	2.0303	44.59	44.63	0.63
106	1.8396	49.51	49.55	15.76
008	1.8025	50.60	50.64	0.22
107	1.6713	54.89	54.94	0.04
110	1.6505	55.64	55.69	20.54
112	1.6089	57.21	57.26	0.12
108	1.5247	60.69	60.75	0.03
114	1.5007	61.77	61.83	0.21
0010	1.4420	64.58	64.64	0.00
200	1.4294	65.22	65.28	2.57
201	1.4224	65.58	65.64	0.10
202	1.4021	66.65	66.72	0.13
109	1.3977	66.89	66.95	16.19
203	1.3701	68.42	68.49	15.21
116	1.3605	68.97	69.03	18.54
204	1.3287	70.86	70.93	0.00
1010	1.2875	73.50	73.57	0.03
205	1.2807	73.95	74.02	0.15
206	1.2285	77.66	77.74	3.98
118	1.2173	78.52	78.59	0.35
0012	1.2017	79.74	79.82	2.32
1011	1.1916	80.55	80.63	0.21
207	1.1744	81.98	82.07	0.02
208	1.1200	86.91	87.00	0.01
1012	1.1078	88.11	88.20	2.31

Table S3. The d-spacings, 2θ angles, and relative intensities of all (*hkl*) reflections based on the individual Rietveld-refined diffraction profiles of $(Zr,Ti)_2(Al,Sn,Pb)C$ in Pb1500.

(*hkl*)	d [Å]	$2\theta_{calc}$ [°]	$2\theta_{exp}$ [°]	I/I_{max} [%]
002	7.2161	12.26	12.27	0.51
004	3.6081	24.65	24.68	0.61
100	2.8629	31.22	31.24	21.37
101	2.8082	31.84	31.87	0.86
102	2.6611	33.65	33.68	1.32
103	2.4602	36.49	36.52	100.00
006	2.4054	37.35	37.39	19.19
104	2.2427	40.18	40.21	0.02
105	2.0326	44.54	44.58	0.84
106	1.8416	49.45	49.50	15.71
008	1.8040	50.55	50.60	0.27
107	1.6731	54.83	54.88	0.07
110	1.6529	55.55	55.61	20.64
112	1.6112	57.12	57.18	0.20
108	1.5263	60.62	60.68	0.06
114	1.5027	61.68	61.73	0.26
0010	1.4432	64.52	64.58	0.00
200	1.4314	65.11	65.17	2.62
201	1.4245	65.47	65.53	0.13
202	1.4041	66.54	66.61	0.15
109	1.3991	66.81	66.88	16.35
203	1.3720	68.31	68.38	15.41
116	1.3623	68.87	68.93	18.84
204	1.3306	70.75	70.82	0.00
1010	1.2887	73.41	73.49	0.03
205	1.2824	73.84	73.91	0.20
206	1.2301	77.54	77.62	4.01
118	1.2187	78.41	78.48	0.44
0012	1.2027	79.66	79.74	2.34
1011	1.1927	80.46	80.54	0.29
207	1.1758	81.86	81.94	0.03
208	1.1213	86.78	86.87	0.03
1012	1.1088	88.01	88.10	2.36

Table S4. Vapor pressure (P_{vap}) of relevant elements at the processing temperatures used in this work, according to Honig, R.E. Vapor Pressure Data for the More Common Elements. *RCA Review* **1957**, 18, 195-204.

Element	P_{vap} **[hPa] at 1350°C**	P_{vap}**[hPa] at 1450°C**	P_{vap}**[hPa] at 1500°C**
Carbon (C)	$< 10^{-8}$	$< 10^{-8}$	$< 10^{-8}$
Aluminum (Al)	0.09	0.53	0.93
Titanium (Ti)	3×10^{-5}	2×10^{-4}	6×10^{-4}
Zinc (Zn)	Boils at 907°C	Boils at 907°C	Boils at 907°C
Zirconium (Zr)	$< 10^{-8}$	$< 10^{-8}$	2×10^{-8}
Tin (Sn)	0.08	0.27	0.47
Lead (Pb)	67	200	270
Bismuth (Bi)	270	600	800

Table S5. The d-spacings, 2θ angles, and relative intensities of all (*hkl*) reflections based on the individual Rietveld-refined diffraction profiles of $(Zr,Ti)_2(Al,Sn,Pb,Bi)C$ in LBE1350.

(*hkl*)	d [Å]	$2\theta_{calc}$ [°]	$2\theta_{exp}$ [°]	I/I_{max} [%]
002	7.2218	12.25	12.26	0.86
004	3.6109	24.63	24.66	0.95
100	2.8769	31.06	31.09	21.10
101	2.8215	31.69	31.71	1.42
102	2.6726	33.50	33.53	1.79
103	2.4696	36.35	36.38	100.00
006	2.4073	37.32	37.36	18.90
104	2.2501	40.04	40.07	0.01
105	2.0384	44.41	44.45	1.20
106	1.8462	49.32	49.36	15.82
008	1.8054	50.51	50.56	0.36
107	1.6767	54.70	54.75	0.16
110	1.6610	55.26	55.31	20.85
112	1.6187	56.83	56.88	0.35
108	1.5292	60.49	60.55	0.09
114	1.5090	61.39	61.45	0.47
0010	1.4444	64.46	64.52	0.00
200	1.4384	64.76	64.82	2.61
201	1.4314	65.12	65.18	0.24
202	1.4107	66.19	66.25	0.23
109	1.4015	66.68	66.75	16.27
203	1.3782	67.96	68.02	15.47
116	1.3671	68.59	68.65	18.76
204	1.3363	70.40	70.47	0.01
1010	1.2908	73.28	73.35	0.07
205	1.2876	73.49	73.56	0.31
206	1.2348	77.19	77.27	4.04
118	1.2224	78.12	78.20	0.62
0012	1.2036	79.58	79.66	2.32
1011	1.1945	80.31	80.39	0.40
207	1.1800	81.51	81.59	0.07
208	1.1250	86.42	86.51	0.04
1012	1.1104	87.85	87.95	2.32
1110	1.0899	89.94	90.00	0.02

Table S6. The d-spacings, 2θ angles, and relative intensities of all (*hkl*) reflections based on the individual Rietveld-refined diffraction profiles of $(Zr,Ti)_2(Al,Sn,Pb,Bi)C$ in LBE1450.

(*hkl*)	d [Å]	$2\theta_{calc}$ [°]	$2\theta_{exp}$ [°]	I/I_{max} [%]
002	7.2159	12.26	12.27	1.28
004	3.6079	24.66	24.68	1.03
100	2.8719	31.12	31.14	21.68
101	2.8167	31.74	31.77	1.65
102	2.6683	33.56	33.59	1.59
103	2.4659	36.41	36.44	100.00
006	2.4053	37.36	37.39	19.24
104	2.2470	40.10	40.13	0.03
105	2.0358	44.47	44.51	1.14
106	1.8440	49.38	49.43	15.62
008	1.8040	50.56	50.60	0.31
107	1.6748	54.77	54.82	0.23
110	1.6581	55.36	55.42	20.83
112	1.6160	56.94	56.99	0.39
108	1.5276	60.56	60.62	0.09
114	1.5066	61.50	61.56	0.49
0010	1.4432	64.52	64.58	0.01
200	1.4360	64.88	64.94	2.71
201	1.4289	65.24	65.30	0.26
202	1.4083	66.32	66.38	0.20
109	1.4001	66.76	66.82	16.64
203	1.3760	68.09	68.15	15.76
116	1.3652	68.70	68.77	19.37
204	1.3342	70.53	70.60	0.02
1010	1.2895	73.36	73.43	0.07
205	1.2856	73.62	73.69	0.29
206	1.2330	77.33	77.41	4.07
118	1.2208	78.25	78.33	0.53
0012	1.2026	79.66	79.74	2.38
1011	1.1933	80.41	80.49	0.33
207	1.1783	81.65	81.73	0.09
208	1.1235	86.57	86.66	0.04
1012	1.1093	87.96	88.05	2.46

Table S7. The d-spacings, 2θ angles, and relative intensities of all (*hkl*) reflections based on the individual Rietveld-refined diffraction profiles of $(Zr,Ti)_2(Al,Sn,Pb,Bi)C$ in LBE1500.

(*hkl*)	d [Å]	$2\theta_{calc}$ [°]	$2\theta_{exp}$ [°]	I/I_{max} [%]
002	7.2161	12.26	12.27	0.92
004	3.6080	24.65	24.68	0.85
100	2.8747	31.09	31.11	21.28
101	2.8193	31.71	31.74	1.28
102	2.6706	33.53	33.56	1.66
103	2.4677	36.38	36.41	100.00
006	2.4054	37.36	37.39	18.96
104	2.2483	40.07	40.11	0.01
105	2.0368	44.44	44.48	1.12
106	1.8447	49.36	49.41	15.70
008	1.8040	50.55	50.60	0.34
107	1.6754	54.75	54.80	0.12
110	1.6597	55.31	55.36	20.73
112	1.6175	56.88	56.93	0.30
108	1.5280	60.54	60.60	0.08
114	1.5078	61.44	61.50	0.37
0010	1.4432	64.52	64.58	0.00
200	1.4373	64.81	64.87	2.61
201	1.4303	65.17	65.24	0.20
202	1.4096	66.25	66.31	0.20
109	1.4004	66.74	66.80	16.16
203	1.3772	68.02	68.08	15.39
116	1.3661	68.65	68.72	18.69
204	1.3353	70.46	70.53	0.01
1010	1.2898	73.34	73.42	0.05
205	1.2866	73.55	73.63	0.27
206	1.2338	77.26	77.34	4.00
118	1.2214	78.20	78.28	0.56
0012	1.2027	79.66	79.74	2.30
1011	1.1936	80.39	80.47	0.37
207	1.1791	81.58	81.67	0.04
208	1.1242	86.51	86.60	0.04
1012	1.1095	87.94	88.03	2.31

Table S8. The d-spacings, 2θ angles, and relative intensities of all (*hkl*) reflections based on the individual Rietveld-refined diffraction profiles of $(Zr,Ti)_2(Al,Sn,Pb,Bi)C$ in Zn1350.

(*hkl*)	d [Å]	$2\theta_{calc}$ [°]	$2\theta_{exp}$ [°]	I/I_{max} [%]
002	7.2080	12.27	12.28	1.04
004	3.6040	24.68	24.70	1.01
100	2.8736	31.10	31.12	21.03
101	2.8182	31.73	31.75	1.49
102	2.6693	33.55	33.57	1.91
103	2.4663	36.40	36.43	100.00
006	2.4027	37.40	37.43	18.79
104	2.2468	40.10	40.14	0.01
105	2.0353	44.48	44.52	1.25
106	1.8433	49.40	49.45	15.76
008	1.8020	50.61	50.66	0.38
107	1.6739	54.80	54.85	0.15
110	1.6591	55.33	55.38	20.68
112	1.6168	56.91	56.96	0.34
108	1.5267	60.60	60.66	0.09
114	1.5071	61.48	61.54	0.44
0010	1.4416	64.60	64.66	0.00
200	1.4368	64.84	64.90	2.55
201	1.4297	65.20	65.26	0.23
202	1.4091	66.28	66.34	0.23
109	1.3991	66.81	66.88	15.93
203	1.3766	68.05	68.12	15.18
116	1.3652	68.70	68.76	18.32
204	1.3347	70.50	70.57	0.01
1010	1.2886	73.43	73.50	0.06
205	1.2860	73.60	73.67	0.30
206	1.2331	77.32	77.39	3.97
118	1.2206	78.26	78.34	0.62
0012	1.2013	79.76	79.84	2.26
1011	1.1924	80.48	80.56	0.40
207	1.1784	81.64	81.73	0.05
208	1.1234	86.58	86.67	0.04
1012	1.1084	88.05	88.14	2.23

Table S9. The d-spacings, 2θ angles, and relative intensities of all (*hkl*) reflections based on the individual Rietveld-refined diffraction profiles of $(Zr,Ti)_3(Al,Sn,Pb,Bi)C_2$ in Zn1350.

(*hkl*)	d [Å]	$2\theta_{calc}$ [°]	$2\theta_{exp}$ [°]	I/I_{max} [%]
002	9.8631	8.96	8.97	0.55
004	4.9316	17.97	17.99	0.73
006	3.2877	27.10	27.12	0.59
100	2.8805	31.02	31.05	9.56
101	2.8503	31.36	31.39	15.37
102	2.7650	32.35	32.38	2.21
103	2.6385	33.95	33.98	7.05
104	2.4873	36.08	36.11	100.00
008	2.4658	36.41	36.44	22.61
105	2.3264	38.67	38.71	17.20
106	2.1666	41.65	41.69	0.79
107	2.0144	44.96	45.00	4.67
0010	1.9726	45.97	46.01	0.58
108	1.8732	48.56	48.61	9.00
109	1.7443	52.41	52.46	7.21
110	1.6631	55.18	55.23	26.08
0012	1.6439	55.89	55.94	0.19
112	1.6399	56.03	56.08	0.26
1010	1.6276	56.50	56.55	0.07
114	1.5759	58.52	58.58	0.37
1011	1.5224	60.79	60.85	2.18
116	1.4840	62.54	62.60	0.31
200	1.4403	64.66	64.73	1.29
201	1.4365	64.86	64.92	1.79
1012	1.4277	65.30	65.36	15.35
202	1.4252	65.44	65.50	0.34
0014	1.4090	66.28	66.34	0.03
203	1.4069	66.39	66.46	1.05
204	1.3825	67.72	67.79	14.87
118	1.3788	67.93	67.99	21.06
205	1.3529	69.41	69.48	2.59
1013	1.3425	70.03	70.09	2.09
206	1.3192	71.45	71.52	0.24
207	1.2825	73.83	73.90	0.97
1110	1.2715	74.58	74.65	0.86
1014	1.2657	74.98	75.05	0.74
108	1.2437	76.54	76.62	2.31
0016	1.2329	77.33	77.41	2.81
209	1.2037	79.58	79.66	1.92
1015	1.1963	80.17	80.25	0.53
1112	1.1691	82.43	82.51	0.40
2010	1.1632	82.94	83.02	0.04
1016	1.1334	85.63	85.72	1.43
2011	1.1229	86.62	86.71	0.76
0018	1.0959	89.32	89.41	0.16

Table S10. The d-spacings, 2θ angles, and relative intensities of all (*hkl*) reflections based on the individual Rietveld-refined diffraction profiles of $(Zr,Ti)_2(Al,Sn,Pb,Bi)C$ in Zn1450.

(*hkl*)	d [Å]	$2\theta_{calc}$ [°]	$2\theta_{exp}$ [°]	I/I_{max} [%]
002	7.2247	12.24	12.25	1.11
004	3.6123	24.62	24.65	1.37
100	2.8779	31.05	31.08	20.58
101	2.8225	31.68	31.70	1.85
102	2.6736	33.49	33.52	2.26
103	2.4705	36.34	36.37	100.00
006	2.4082	37.31	37.34	18.63
104	2.2509	40.02	40.06	0.01
105	2.0392	44.39	44.43	1.33
106	1.8469	49.30	49.34	15.93
008	1.8062	50.49	50.53	0.40
107	1.6773	54.68	54.73	0.24
110	1.6616	55.24	55.29	20.60
112	1.6193	56.81	56.86	0.37
108	1.5298	60.47	60.52	0.08
114	1.5095	61.37	61.42	0.60
0010	1.4449	64.43	64.49	0.01
200	1.4390	64.73	64.79	2.46
201	1.4319	65.09	65.15	0.28
202	1.4112	66.16	66.23	0.26
109	1.4021	66.65	66.72	15.68
203	1.3787	67.93	68.00	14.88
116	1.3676	68.56	68.63	17.81
204	1.3368	70.37	70.44	0.01
1010	1.2913	73.24	73.31	0.09
205	1.2881	73.45	73.53	0.33
206	1.2352	77.16	77.24	3.93
118	1.2228	78.09	78.17	0.65
0012	1.2041	79.54	79.62	2.23
1011	1.1950	80.27	80.35	0.39
207	1.1804	81.47	81.55	0.09
208	1.1255	86.38	86.47	0.03
1012	1.1108	87.81	87.90	2.13

Table S11. The d-spacings, 2θ angles, and relative intensities of all (*hkl*) reflections based on the individual Rietveld-refined diffraction profiles of $(Zr,Ti)_2(Al,Sn,Pb,Bi)C$ in Zn1500.

(*hkl*)	d [Å]	$2\theta_{calc}$ [°]	$2\theta_{exp}$ [°]	I/I_{max} [%]
002	7.2157	12.26	12.27	1.07
004	3.6079	24.66	24.68	1.16
100	2.8735	31.10	31.13	21.44
101	2.8182	31.73	31.75	1.64
102	2.6696	33.54	33.57	1.63
103	2.4669	36.39	36.42	100.00
006	2.4052	37.36	37.39	19.09
104	2.2477	40.08	40.12	0.03
105	2.0364	44.45	44.49	1.00
106	1.8444	49.37	49.42	15.67
008	1.8039	50.56	50.60	0.27
107	1.6751	54.76	54.81	0.26
110	1.6590	55.33	55.38	20.71
112	1.6168	56.90	56.96	0.33
108	1.5278	60.55	60.61	0.06
114	1.5073	61.47	61.52	0.52
0010	1.4431	64.52	64.58	0.01
200	1.4368	64.84	64.90	2.64
201	1.4297	65.20	65.26	0.24
202	1.4091	66.28	66.34	0.19
109	1.4002	66.75	66.81	16.35
203	1.3767	68.05	68.11	15.47
116	1.3657	68.67	68.74	18.90
204	1.3348	70.49	70.56	0.01
1010	1.2896	73.35	73.43	0.09
205	1.2862	73.58	73.65	0.24
206	1.2335	77.29	77.37	4.01
118	1.2211	78.22	78.30	0.45
0012	1.2026	79.66	79.74	2.34
1011	1.1934	80.40	80.48	0.26
207	1.1788	81.61	81.69	0.09
208	1.1239	86.53	86.63	0.03
1012	1.1094	87.95	88.04	2.37

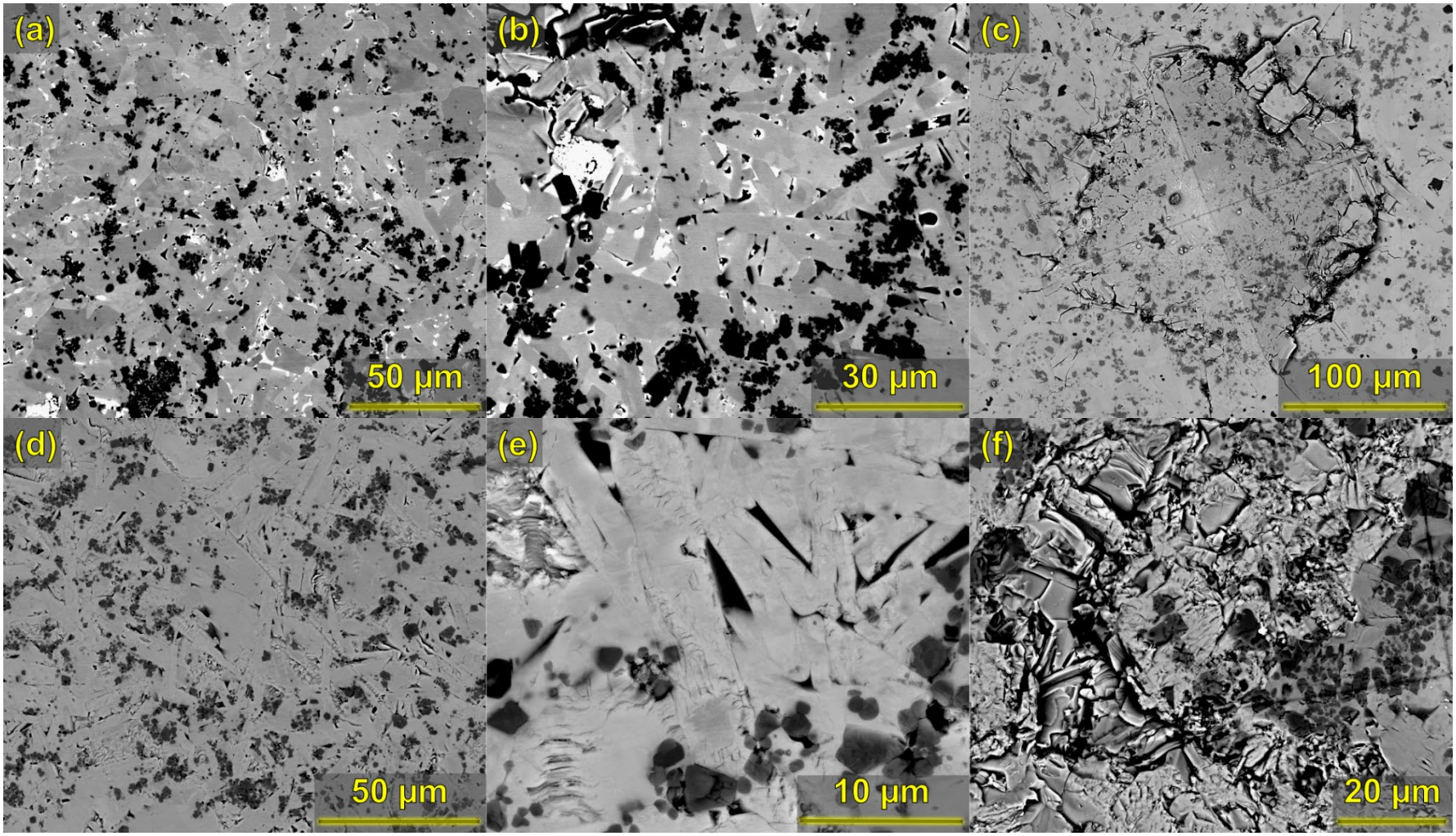

Figure S1. SEM analysis (BSE, 20 kV) of the Pb1450 ceramic revealed (a,b) characteristic MAX phase platelets (grey), clusters of (Zr,Ti)C (black), and intergranular heavy metal-enriched IMC GB phase (bright); and (c) MAX phase delamination near a Vickers indentation preventing crack formation. SEM analysis (BSE, 20 kV) of the Pb1500 ceramic revealed (d,e) MAX phase platelets (grey) and clustered (Zr,Ti)C (black) without distinctive IMC GB phase; and (f) the MAX phase absorbing damage through delamination near a Vickers indentation.

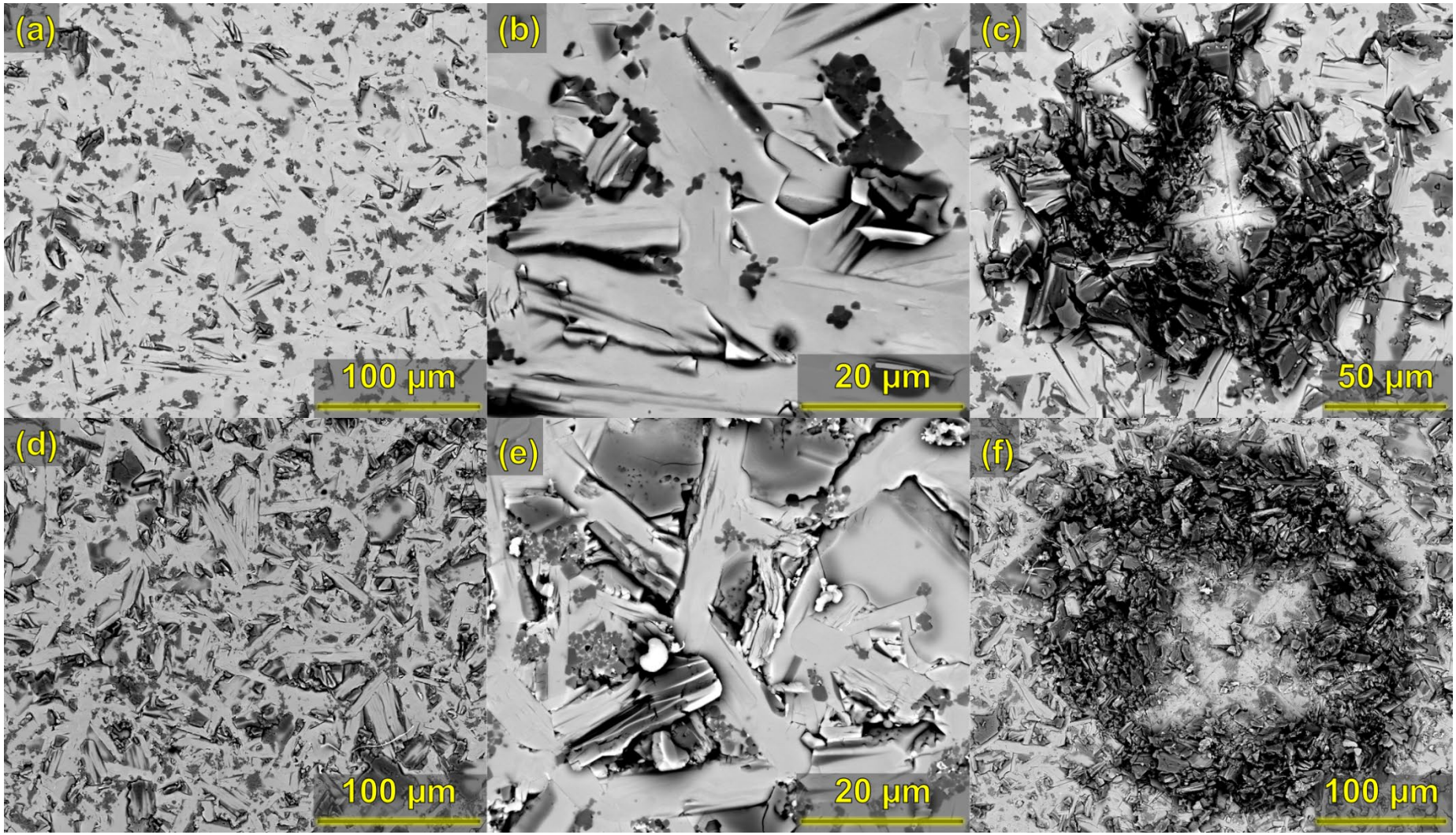

Figure S2. SEM analysis (BSE, 20 kV) of the LBE1350 ceramic revealed (a,b) MAX phase platelets (grey) and clusters of (Zr,Ti)C (black); and (c) pronounced MAX phase delamination near a Vickers indentation. SEM analysis (BSE, 20 kV) of the LBE1500 ceramic revealed (d,e) MAX phase platelets (grey), clustered (Zr,Ti)C (black), and LBE particles (bright); and (f) damage absorption by MAX phase delamination near a Vickers indentation.

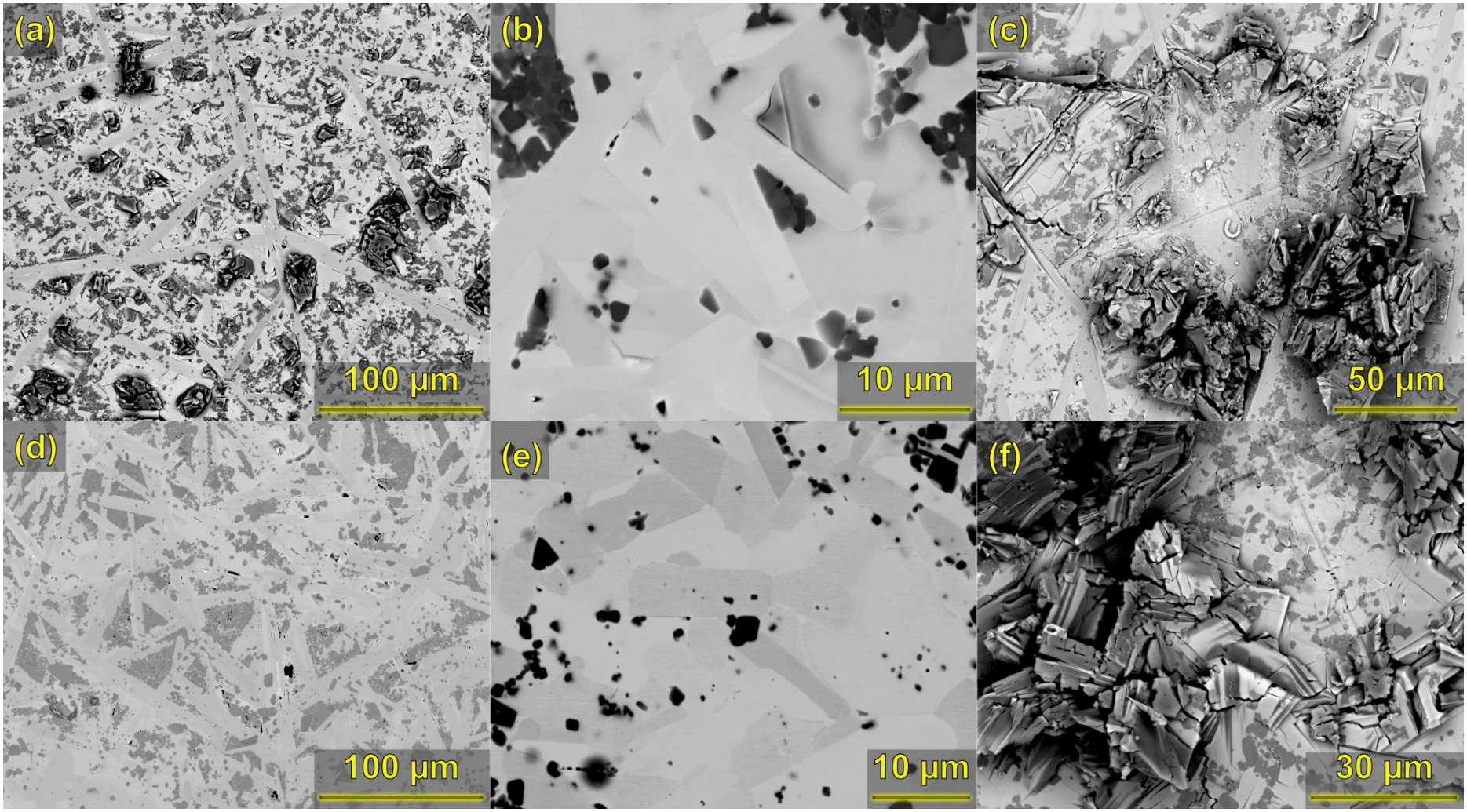

Figure S3. SEM analysis (BSE, 20 kV) of the Zn1450 ceramic revealed (a,b) bimodal MAX phase platelets (grey), and clusters of (Zr,Ti)C (black); and (c) MAX phase delamination & crack deflection near a Vickers indentation. SEM analysis (BSE, 20 kV) of the Zn1500 ceramic revealed (d,e) MAX phase platelets (grey) with (Zr,Ti)C (black) filling intergranular junctions; and (f) MAX phase delamination & crack deflection near a Vickers indentation.